Residual Stresses In Circular Thin Plates Using Two Dimensional X-ray Diffraction And Finite Element Analysis

by

Mohammed Alusail

A thesis

presented to the University of Waterloo

in fulfillment of the

thesis requirement for the degree of

Master of Applied Science

in

Mechanical Engineering

Waterloo, Ontario, Canada, 2013

AUTHOR'S DECLARATION

I hereby declare that I am the sole author of this thesis. This is a true copy of the thesis, including any required final revisions, as accepted by my examiners.

I understand that my thesis may be made electronically available to the public.

Mohammed Alusail

Abstract

There are many causes of structural failure. One of the most important factors leading to material failure is residual stress. This stress represents effects left in structures after processing or removal of external loads including changes in shape and crystallite size. In aggregate, residual stress changes the mechanical behaviour of materials. Various measurement techniques encompassing destructive, semi destructive, and non-destructive testing can be used to measure residual stresses.

Thin plates are common in engineering applications. This thesis analyzes residual stresses on circular AISI 1020 steel alloy plates after removal of external loads using two-dimensional X-ray diffraction. Two identical thin circular plates are used in this experiment; one of which is statically loaded. The other plate is used as a control specimen. Residual stresses in the plates are measured using two-dimensional X-ray diffraction and the measurements are compared to those obtained using finite element analysis. It was found that experimentally measured residual stress occurred due to manufacture processing. Also, modules A and B showed the external effect of applying not enough to reach the plastic region to deform specimen 2 and obtain residual stress results distribution.

Acknowledgements

I am ever thankful to Allah for all things. Although I have been challenged by difficulties in life, but I always say Alhamdulillah.

However much I thank my parents, I cannot thank them enough. They raised me with love and taught me to gain more knowledge in this world. They have always encouraged me to move forward in this life.

I am very grateful for my country Saudi Arabia, which has formed the foundation of my life and has also given me a full scholarship to come to Canada to study. Without the support of Saudi Arabia, it would have been impossible for me to conduct this research. Many thanks to the King of Saudi Arabia Abdullah bin Abdulaziz Al Saud.

I thank Dr. Mustafa Yavuz, my supervisor during this research. He has consistently given me his time and focus during our regular meetings. He has treated me with kindness, provided me with great knowledge, and encouraged me to persevere. I am very fortunate to be one of his students at the University of Waterloo. I also thank Dr. Eihab M. Abdel-Rahman, my co-supervisor during this research. Dr. Abdel-Rahman helped me to solve problems I encountered and facilitated my deeper understanding of finite element analysis. Thank you to Dr. Hamid Jahedmotlagh, Associate Chair of Graduate Studies who demonstrated understanding of my problem and gave me another opportunity to continue my Master of Applied Science.

I cannot forget to thank every one of my friends who supported me. Thank you to author Bob Baoping, who wrote the *Two-dimensionalX-ray Diffraction* textbook. This book has remained with me through my entire Master's study due to its great knowledge.

Finally, I have learned that all is possible if I trust myself and work hard. Failure is only the beginning of success. I have found that whatever I gain from learning, there is even more to learn. In life there is no limit to knowledge.

Dedication

To my parents and my country Saudi Arabia

I dedicate this thesis

Table of Contents

List of Figures

List of Tables

Chapter 1

Introduction

1.1 Motivation

There are many causes of failure in structures. One important effect on a material structure is stress. This thesis focussed on residual stresses in thin plate structures. Residual stress is the stress left in structures after the removal of external loads. There are two levels of residual stresses, which are micro and macro. Residual stresses may occur in many manufactured structures and components without external loading.

Internal stress or residual stress cannot be detected simply through visual observation. Therefore, measurement techniques such as destructive, semi destructive and non-destructive testing, are used to detect and measure residual stresses. Destructive testing completely damages the material by cutting the sample into different parts. Semi destructive testing cuts a part of material to calculate residual stresses. In non-destructive testing, residual stresses are measured without damaging the material. Figure 1.1 shows some of these techniques, and Table 1.1 provides their advantages and disadvantages [1]. One of the most important non-destructive testing techniques is X-ray diffraction.

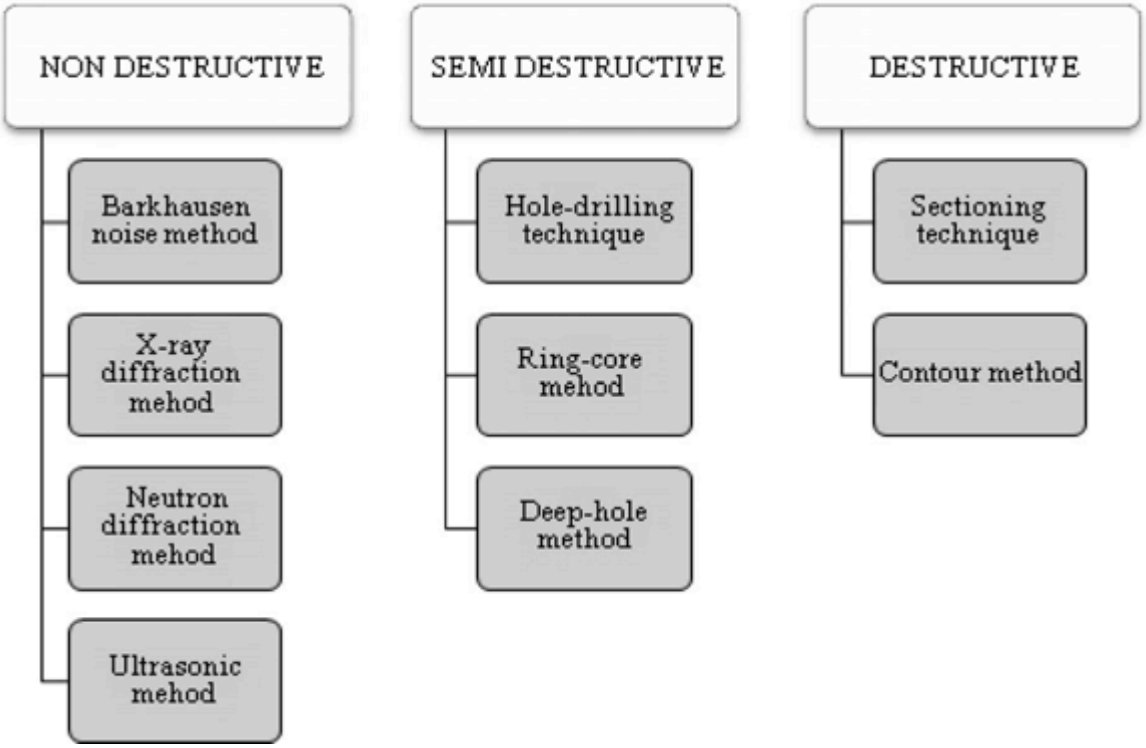

Figure 1:1: Residual stresses measurement techniques [1].

Table 1.1: Advantages and disadvantages of measurement techniques [1].

Technique	Advantages	Disadvantages
Diffraction	Ductile material Varied range of materials Macro and Micro	Lab-based Systems Expensive
Ultrasonic	Very quick Low cost	Limited resolution Bulk measurements over whole volume
Neutron Diffraction	Macro and Micro	Offered by few facility Lab-based system

Barkhausen Noise	Fast High sensitivity to microstructure effects especially in welds	Only ferromagnetic materials Need to separate the microstructure signal from that due to stress
Hole Drilling	Very quick Easy to use Varied range of materials	Semi destructive testing Limite to strain
Sectioning	Wide range of materials Inexpensive Very quick	Destructive testing Limited to strain
Synchrotron	Improved penetration and resolution ofX-rays Very quick Macro and micro	Offered by few facility Lab-based systems Expensive

This research focuses on measurement of residual stress using two-dimensional X-ray diffraction and finite element analysis. These two techniques are very powerful and distinct, which makes it a very challenging field of study.

In this thesis, there are five chapters: chapter 1 introduces two X-ray diffraction, chapter 2 defines residual stresses obtained using two-dimensional X-ray diffraction, chapter 3 describes the LEPTOS software, chapter 4 covers the use finite element analysis to calculate residual stresses, and chapter 5 provides the results and discusses them.

1.2 History ofX-rays

Wilhelm Conrad Röntgen discovered X-rays in 1895. In fact some textbooks refer to X-rays as Röntgen radiation. He was honoured with the Nobel Prize for Physics in 1901 [2]. Unlike light,

X-ray radiation has the ability to discover what the human eyes cannot see. Since then, X-ray technology has developed to involve many research areas such as medical and engineering applications. X-ray based study of crystals was introduced in 1912 by Max Von Laue. One of the most important mathematical formulae governing X-ray was noticed by Bragg, namely Bragg's law for which he was awarded the Nobel prize for Physics in 1915. The firstX-ray diffraction was used by W. H. and W. L. Bragg. X-ray powder diffraction and other x ray diffraction types collect data from one-dimensional diffraction lines. One-dimensional diffraction lines collect the data with scanning point detectors or linear position-sensitive detectors (PSD) [3]. These types of X ray diffraction are collected by conventional diffractometers [3]. Since 1999, two-dimensional X-ray theory and application had been discovered. The X-ray diffraction is used for phase identification, thin films, texture analysis, and stress measurement.

1.3 X-ray Radiation

X-rays refer to a region in the electromagnetic radiation spectrum that have a very short wavelength compared to other electromagnetic waves as shown in Figure 1.2 [4]. X-ray radiation wavelengths are on the order of one angstrom (A), which is equal to 10^{-8} cm [4]. As shown in Figure 1.2, X-rays occur between Gamma- rays and ultraviolet. This type of light has the ability to show the internal details of materials that other radiation cannot.

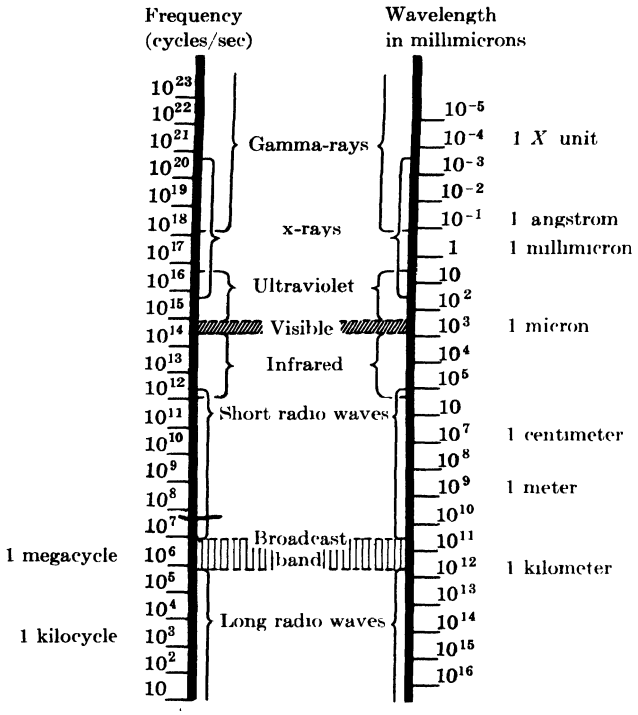

Figure 1:2: Electromagnetic radiation spectrum [4].

1.4 X-ray Diffraction

When the X-ray incident beam reaches a specimen, the X-rays are reflected through diffraction. This kind of diffraction is called elastic scattering. The atomic distribution in a specimen might be disordered such as glass or ordered like single silicon [2]. The structure can by calculate by the intensity, spatial distributions and diffraction pattern of the reflected X-rays. X-ray diffraction is able to provide atomic distribution of any material.

1.5 Crystal Structure

The crystal X-ray diffraction pattern is able to show the geometry and structure of a crystalline solid. The atomic arrangement is in lattice points in three –dimensions that compose of crystal

planes. The lattice planes are described by Miller indices, which is a set of three integers hkl [2]. The three axes (hkl) are described the orientations planes inside the crystal structure. Some crystal structure reflection rules of X-ray diffraction are shown in Table 1.2 [5].

Table 1.2: Reflection rules of X-ray diffraction [5].

Crystal structure	*Diffraction does not occur for*	*Diffraction occurs for*
BCC	$h + k + l$ = odd number	$h + k + l$ = even number
FCC	h, k, l can have both even and odd integer values	h, k, l can be all even or all odd numbers
HCP	$h + 2k = 3n$, l odd ($n \rightarrow$ integer)	All other cases

1.6 Bragg's Law

Bragg law is one of the most important laws in X-ray diffraction due to the simplicity of its description for the diffraction of X-rays by a crystal. This law explains the relation between material structure and diffraction pattern. It also provides information on incident X-rays, incident angle, and reflection angle, as shown in Figure 1.3. The gray spots are the atomic positions in a strain-free crystal. The horizontal lines connecting them are the crystal planes in the strain-free crystal. Where is d_0 is d- spacing, θ_0 Bragg angle, and ε_n strain direction. The direction changing in d_0 and θ_0 is refer to d and θ. In X-ray diffraction Bragg's law is satisfied when the diffraction peak is shifted.

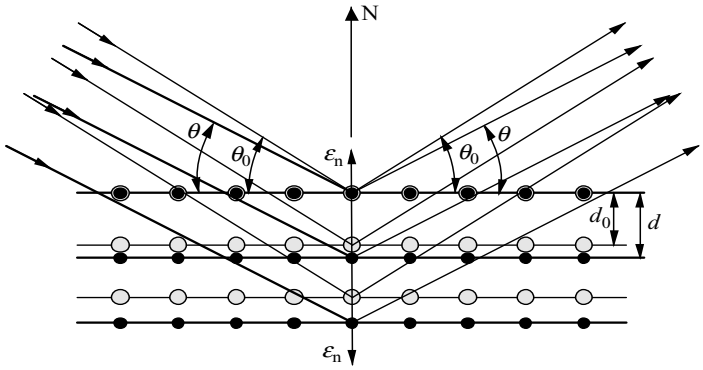

Figure 1:3: Bragg law of strain measurement [2].

$$n\lambda = 2d\sin\theta \tag{1.1}$$

Equation.1.1. Where λ is the wavelength, n is an integer, (d-spacing) is the distance between adjacent crystal planes, and θ_0 is the Bragg angle relative to the incident beam. The strain-free crystal Bragg law is given by equation 1.2. [2]. Also, for a crystal with strain the Bragg law is given by equation 1.3. [2].

$$2d_0 \sin\theta_0 = \lambda \tag{1.2}$$

Free Strain Bragg law [2].

$$2d \sin\theta = \lambda \tag{1.3}$$

Crystal with strain Bragg law [2].

However, the diffracted intensities I at a range of 2θ angles is displayed as diffraction peak [2]. The peak diffraction represent as curved line with highest points which provide intensity maximum, I_{max}. The peak diffraction width measured by its full width at half maximum (FWHM) is shown in Figure 1.4 [2].

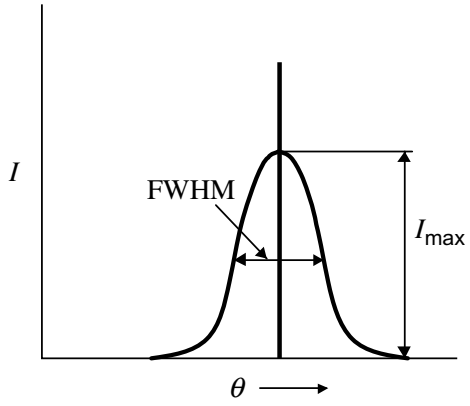

Figure 1:4: the peak diffraction shown Imax and (FWHM) at the Bragg angle θ [2].

The peaks have many shapes fits for crystal planes found by the Bragg law. Bragg's law is satisfied when the crystal has been rotated at various angles during the data collection; therefore, to satisfy Bragg's law the crystal must be in the right orientation [2]. This technique used in the Gandolfi camera is such that the crystal is rotated above an axis tilted 45° from the camera axis [2]. "X-ray diffraction phenomena can also be explained in reciprocal space by the reciprocal lattice and the Ewald sphere" [2].

1.7 The Ewald Sphere

The reciprocal lattice represents the crystal lattice in real space. The Ewald sphere explains the relationship between the Bragg law condition and the reciprocal lattice. This method is a

formation that displays Bragg planes in the correct orientation to cause diffraction, as shown Figure 1.5 [2].

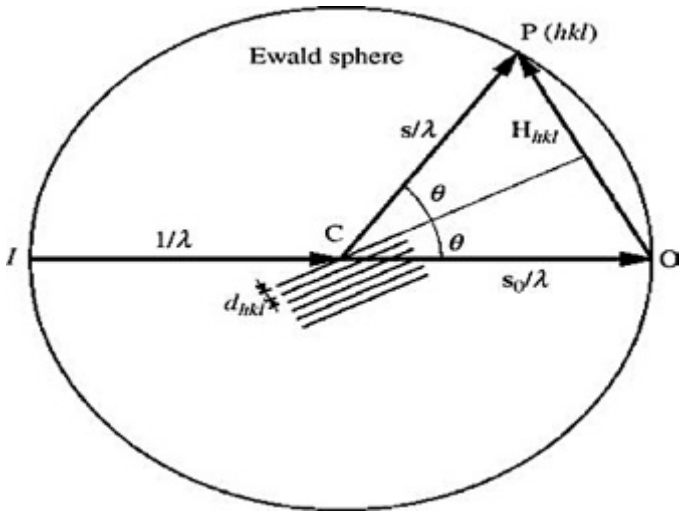

Figure 1:5: Ewald sphere [2].

Where 1/ λ is the radius of the Ewald sphere. The incident beam starts at C at direction s_0/λ and ends at O. The diffracted beam s/ λ starts at the point C and ends at point P. Therefore, the line from O to P is the reciprocal lattice H_{hkl} given. Both beams are at an angle θ from a crystal planes (hkl) with d-spacing of the crystal planes. Equation 1.4 gives the relationship between the Ewald sphere and Bragg law. To satisfy the Bragg law, the reciprocal lattice point must be on the Ewald sphere.

$$\left|\frac{\mathbf{s}-\mathbf{s}_0}{\lambda}\right| = \frac{2\sin\theta}{\lambda} = |\mathbf{H}_{hkl}| = \frac{1}{d_{hkl}} \tag{1.4}$$

Relationship between Ewald sphere and Bragg law [2].

1.8 Two-Dimensional X-ray Diffraction:

The two-dimensional collection of data with an area detector collect the data in less time and provides more data points. The diffraction pattern gathered with an area detector provides a two-dimensional look like a frame. The X-ray intensity becomes like an image diffraction pattern, called a frame. The diffraction frame collected from a corundum powder is shown in Figure 1.6[2]. The two-dimensional X-ray diffraction system has an area detector, sample positioning stage, X-ray source, X-ray optics, sample alignment and monitoring device with computer control to analysis results, as shown in Figure 1.7[6]

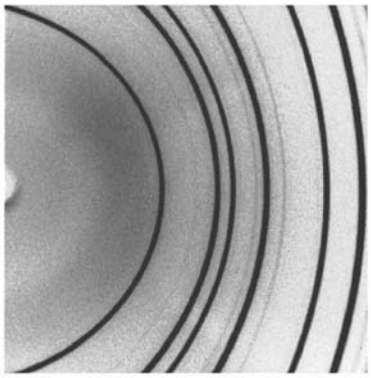

Figure 1:6: Diffraction frames [2].

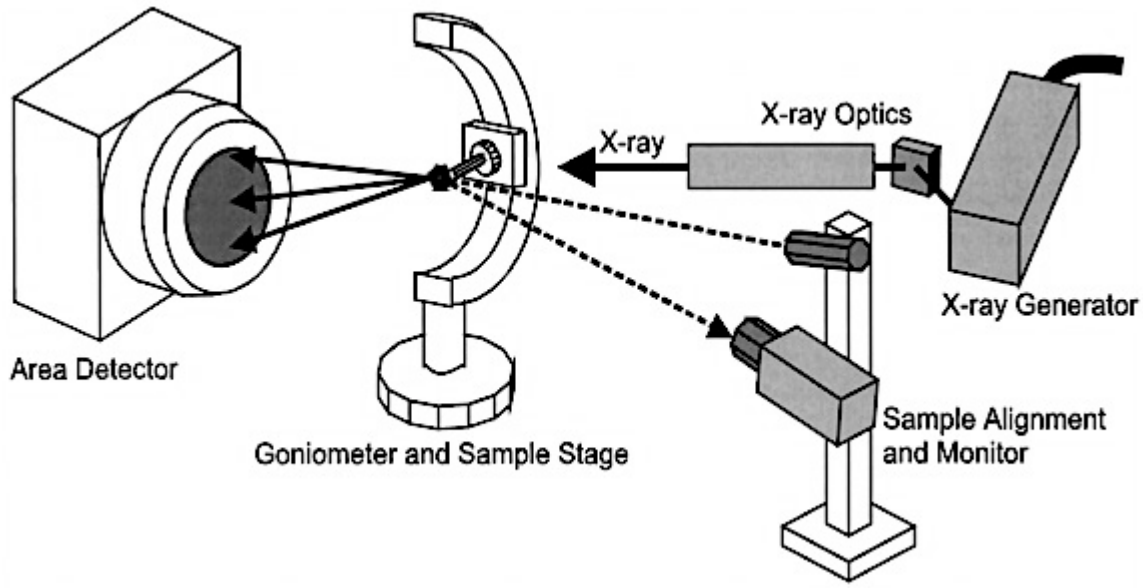

Figure 1:7: The two-dimensional X-ray diffraction system [6].

1.9 Rotations in Two-Dimensional X-ray Diffraction

Two-dimensional X-ray diffraction system consists of three geometry spaces, which are the diffraction space, detector space, and sample space, and the basis of all three spaces coordinate system are the X_L Y_L Z_L directions. The diffraction space represents the beam diffraction (2θ, γ). The detector space is collected the data in direction (D, α). There are many stages samples, which is holding the sample for the experiment. The relation between theses spaces is shown in Figure 1.8. There are two diffraction cones, in which one represents forward diffraction ($2\theta<90°$) and the other backward diffraction ($2\theta>90°$), as shown in Figure1.9 [2]. The X- ray beam direction is X_L, which also represents the rotation axis of the diffraction cones. On the other hand, there are three rotation angles for sample spaces calculate by Eulerian geometry. There are three angles in Eulerian geometry ω (omega), ψ (psi), and ϕ (phi), as shown in Figure

1.9 [2]. The omega angle is fixed in geometric coordinates. However, it is important to assign the coordinates S_1, S_2, and S_3 on sample due to analyze the diffraction results to the sample orientation as shown in Figure 1.10. In addition, Bruker AXS GADDS (General Area Detector Diffraction System) is shown in Figure 1.11.

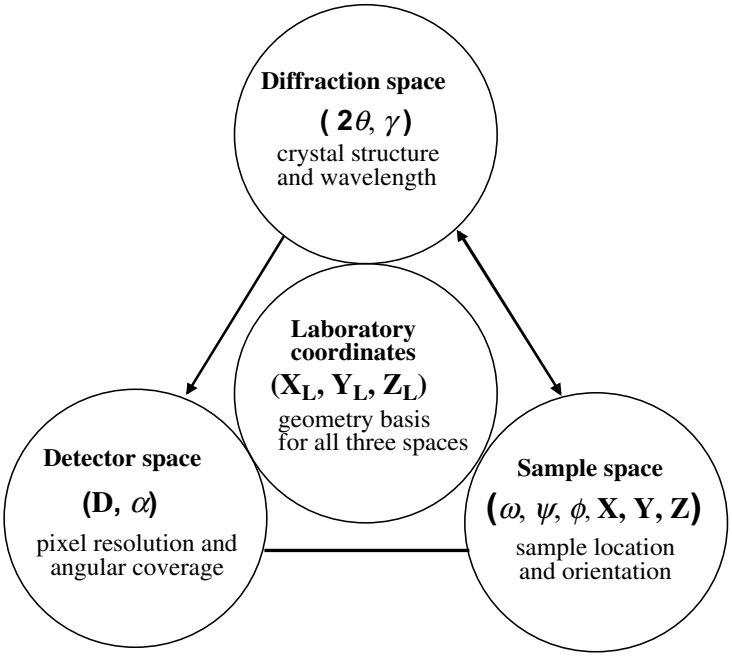

Figure 1:8: diffraction space, detector space, and sample space [2].

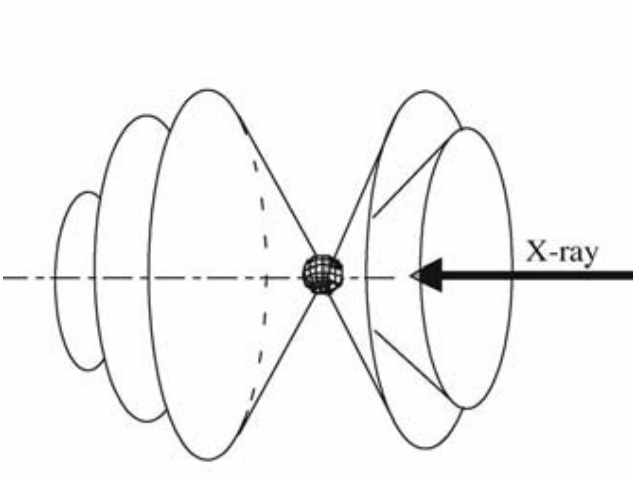

Figure 1:9: Two diffraction cones [2].

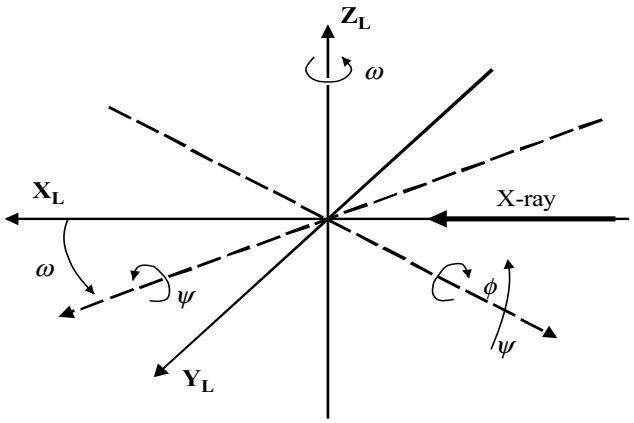

Figure 1:10: Three rotation axes in $X_LY_LZ_L$ coordinates. [2].

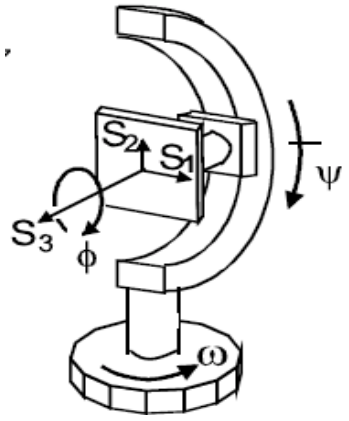

Figure 1:11:Sample coordinates and Eulerian angles [2].

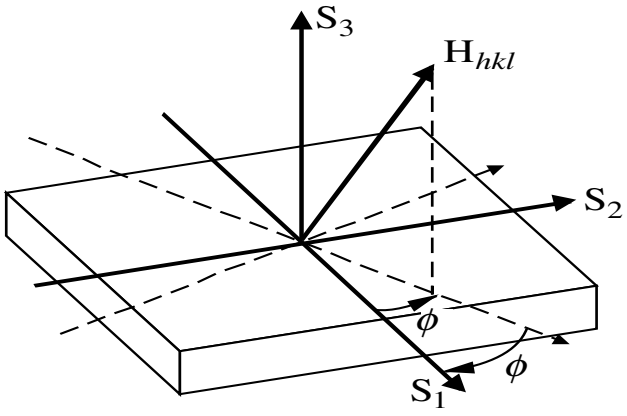

Figure 1:12: Coordinates S_1, S_2, and S_3 [2].

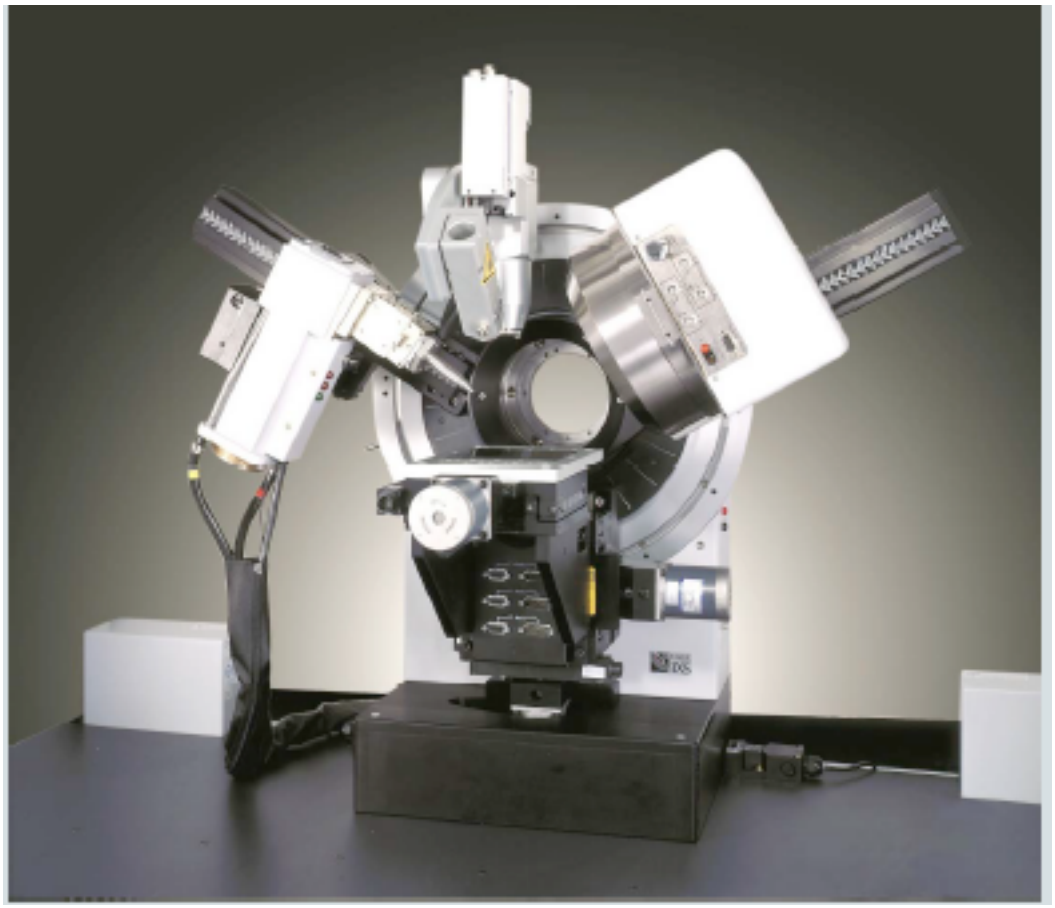

Figure 1:13:Bruker AXS GADDS (General Area Detector Diffraction System) [2].

Chapter 2

Residual Stress Measurement

2.1 INTRODUCTION

Crystallites in a material are changing shape or size because of elastic deformation caused by external loads or in manufacturing process. These changes in the material are called residual stresses. To calculate the residual stresses in each crystallite, the stresses are measured by the change in lattice d-spacing in the crystallites. There are two kinds of stresses in material, either tensile or compressive. Therefore, the d-spacing in the crystallite can be smaller or larger than the stress-free sample. The diffraction peaks can be used to calculate the d-spacing from Bragg's law. The residual stresses cannot be measured by X-ray diffraction [2]. Therefore, the residual stresses can be calculated from strains using the Hooke's law [2]. The diffraction peak 2θ shifts can be use to calculate the residual stress from strain. Changing the orientations (ω, ψ, ϕ) leads to measuring the residual stress from many diffraction peaks. The relationship between the stress tensor and diffraction cone distortion collected with a two-dimensional data detector can be used to solve the stress tensor with an area detector. The peak 2θ shifts are measured along the diffraction ring. However, the two-dimensional X-ray diffraction provides more data points than one-dimensional X-ray diffraction peak, which requires less time for collection. There are three categories of residual stresses relate to the scale of the grain size, as shown in Figure 2.1. The first category is macroscopic residual stress σ_I, which is measured over a large grain area of several millimeters. In addition, this stress can by measured by X-ray diffraction through the shift of the Bragg peaks. The second category is microscopic stress σ_{II}, which is measured from

one grain or a few. If the micro X-ray beam is very small as several grains, this category of stress could shift the diffraction. The last category relates to the strains on severer nanometer σ_{III}. This category of stress cannot be collected from the shift of diffraction peaks, but it can collect by the peak broadening lines [2]. In this thesis, the residual stress σ_I evidenced by two-dimensional X-ray diffraction of the macroscopic residual stress measured over a large grain area of several millimeters is used in this research.

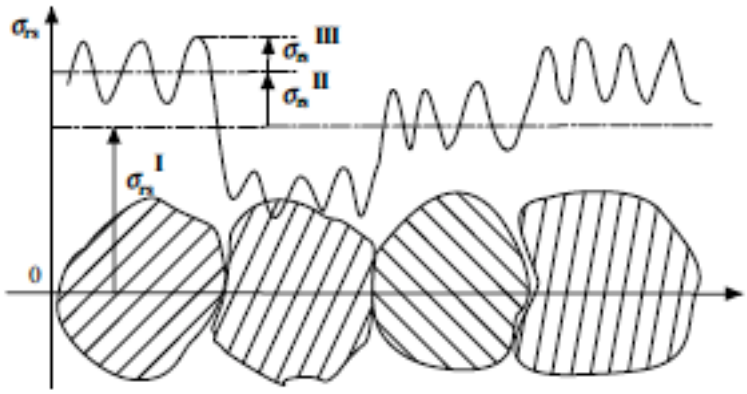

Figure 2:1: Three kinds of residual stresses [2].

2.2 Stress Tensor

Stress measurement is calculated from the deformation force applied over unit area. The stress-strain relationship is shown in Figure 2.2. Also, the force F can be applied to a horizontal area A_0 of a body, as shown in Figure 2.2 (a). The force is classified by two components, which are F_n, normal force and F_t, tangential force. The external force is equal to the internal force. The internal force is called stress. The nine stress components are shown in Figure 2.2 (b). The stress can calculate from equation 2.1. The stress is a tensor of the second order. The normal stress

ellipsoid and principal stresses components are shown in Figure 2.1(c). The strain factors on a volume element are calculated from equation 2.2 and shown in Figure 2.1 (d).

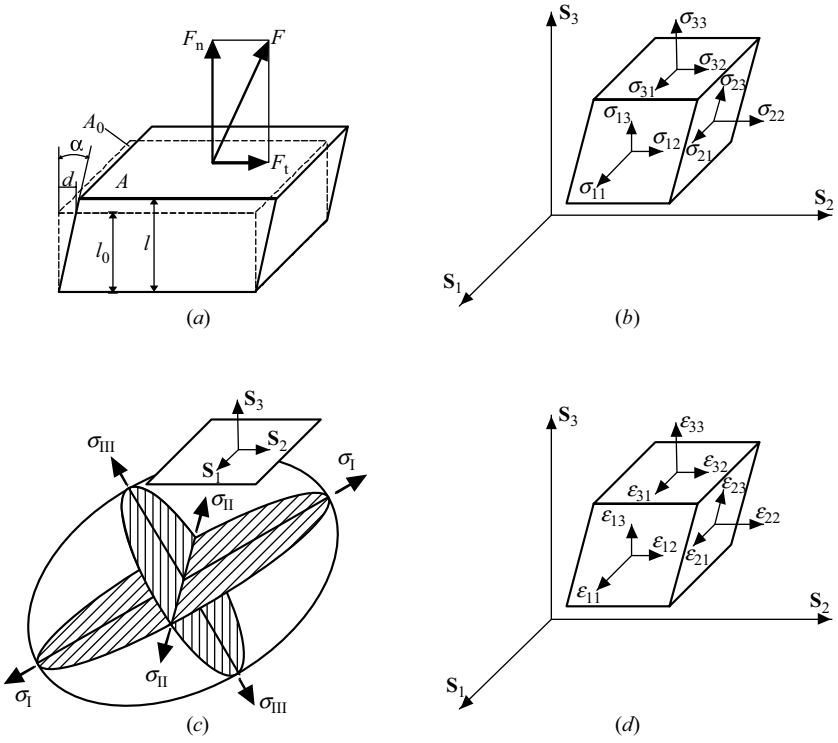

Figure 2:2: Stress measurement [2].

$$\sigma = \frac{F_n}{A_0} \tag{2.1}$$

Where is the normal force F_n, A_0 area and stress σ [2].

However, the nine stress components, corresponding on the coordinates S_1, S_2, and S_3 contains given by equation 2.2 [7].

$$\sigma_{ij} = \begin{bmatrix} \sigma_{11} & \sigma_{12} & \sigma_{13} \\ \sigma_{21} & \sigma_{22} & \sigma_{23} \\ \sigma_{31} & \sigma_{32} & \sigma_{33} \end{bmatrix} \tag{2.2}$$

The indices 1,2 and 3 might be stated as x, y and z, respectively. The two identical indices represent normal stresses. The two mix indices represent shear stress. The stress tensor measurement is second order. There are three normal stress components with the three axes of the specimen coordinates. In addition, there are six shear components within the three axes of the sample coordinates. The stresses states in a solid are six independent components as explained below [2]. In stress analysis σ_3 does not equal zero, because it is in the surface normal direction.

Uniaxial stress:

All shear stresses factors are zero, but the normal stress is not zero.

$$\sigma_{ij} = \begin{bmatrix} \sigma_{11} & 0 & 0 \\ 0 & 0 & 0 \\ 0 & 0 & 0 \end{bmatrix} \text{ or } \sigma_{ij} = \begin{bmatrix} 0 & 0 & 0 \\ 0 & \sigma_{22} & 0 \\ 0 & 0 & 0 \end{bmatrix} \text{ or } \sigma_{ij} = \begin{bmatrix} 0 & 0 & 0 \\ 0 & 0 & 0 \\ 0 & 0 & \sigma_{33} \end{bmatrix}$$

Biaxial:

The normal and shear stress factors are with in a plane, for instance, in the S_1–S_2 plane. There is no balancing force applied in the normal direction of the surface. This type of stress is the most comment measured of stresses by X-ray diffraction, because of the limited permeation of X-rays into the material.

$$\sigma_{ij} = \begin{bmatrix} \sigma_{11} & \sigma_{12} & 0 \\ \sigma_{21} & \sigma_{22} & 0 \\ 0 & 0 & 0 \end{bmatrix}$$

Biaxial with Shear:

The normal and shear stress factors are not zero except σ_3. This type of stress analysis does not need to measure free d-spacing. Also, the triaxial stress state is related to biaxial with shear. However, there is a distinction between a biaxial with shear state and triaxial stress state due to triaxial stress needing accurate stress-free d-spacing. Biaxial with shear stress in the surface normal direction is zero, because of the low permeation of the X-ray.

$$\sigma_{ij} = \begin{bmatrix} \sigma_{11} & \sigma_{12} & \sigma_{13} \\ \sigma_{21} & \sigma_{22} & \sigma_{23} \\ \sigma_{31} & \sigma_{32} & 0 \end{bmatrix}$$

Equibiaxial:

This is another type of the biaxial stress state where σ_{11}, σ_{22} equals σ. There are no shear factors in the equibiaxial, but only normal stress component, which can occur in any direction within the plane with same value. This stress state is especially used for shot peening and thin films. equibiaxial occurs on the surface after surface treatment.

$$\sigma_{ij} = \begin{bmatrix} \sigma & 0 & 0 \\ 0 & \sigma & 0 \\ 0 & 0 & 0 \end{bmatrix}$$

Triaxial:

Triaxial occurs only of metal parts or inside the solid body. This type cannot be calculated from X-ray diffraction directly due to the limited penetration depth of X-rays. It can be measured by layer removal method. This type can be calculated from high-energy X-rays, synchrotron radiation, or neutron radiation. Also, the stress-free d-spacing must be known in order to measure the triaxial stresses due to it being undetermined by measurement of the stress state.

$$\sigma_{ij} = \begin{bmatrix} \sigma_{11} & \sigma_{12} & \sigma_{13} \\ \sigma_{21} & \sigma_{22} & \sigma_{23} \\ \sigma_{31} & \sigma_{32} & \sigma_{33} \end{bmatrix}$$

Equitriaxial:

This is another type of triaxial stress state where σ_{11}, σ_{22},σ_{33} equals σ. Although there are no shear components in the equitriaxial, there is only a normal stress component, which can occur in any direction within the plane sharing the same value. This type of stress state occurs in solid body with uniform forces over the surface of the body normal to any direction on the surface, such as a solid body submerged in a fluid under pressure. As result, this type of stress is indicated as the hydrostatic state [2]. For hydrostatic stresses, no phase transformation exists because of pressure. While equitriaxial seems like a diffraction pattern from a crystal of the same structure, it has a different unit cell size.

$$\sigma_{ij} = \begin{bmatrix} \sigma & 0 & 0 \\ 0 & \sigma & 0 \\ 0 & 0 & \sigma \end{bmatrix}$$

All these types of stress factors are formulated on the coordinates S_1,S_2, and S_3. The stress tensor can be formulated from Cartesian coordinates tilted away from coordinates with different stress components. The three principal stresses, $\sigma_{I,}$ σ_{II}, and σ_{III} are axes of the ellipsoid without shear stress as show in Figure2.2 (c). Also, the three principal stresses have assigned values in the following order. In addition, the relation between the principal axis system and coordinate system is shown in Figure 2.3.

$$\begin{bmatrix} \sigma_I & 0 & 0 \\ 0 & \sigma_{II} & 0 \\ 0 & 0 & \sigma_{III} \end{bmatrix}$$

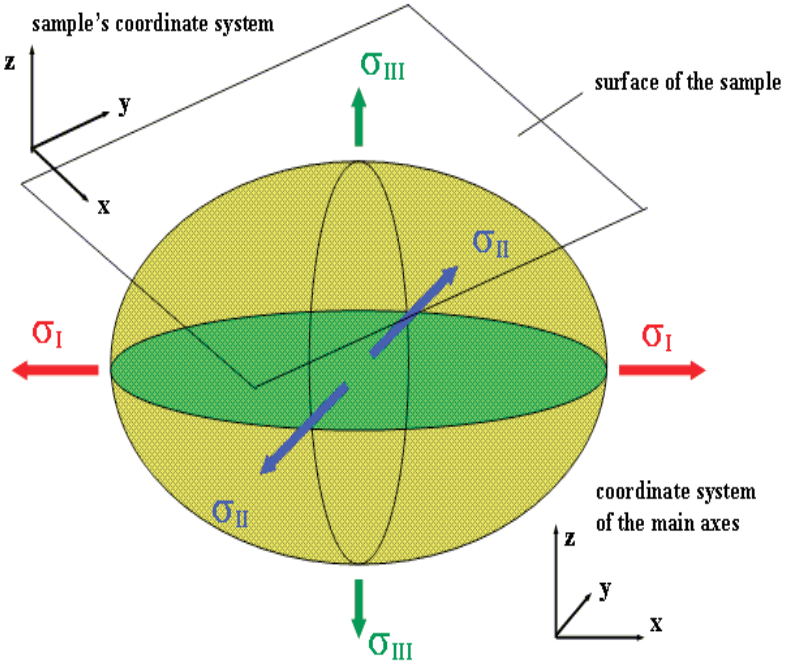

Figure 2:3: Relation between sample's coordinate system and principal axes' system (with tensor ellipsoid) [8].

2.3 Strain Tensor

Strain is calculated from stress deformation of a structure. Therefore, strain is measured from a change in the material, such as in the size or shape. Normal strains and shear strains are analogous to normal stresses and shear stresses. Normal strain is given by equations 2.3.

$$e_{\mathrm{n}} = \frac{l - l_{\mathrm{o}}}{l_{\mathrm{o}}} = \frac{\Delta l}{l_{\mathrm{o}}} \tag{2.3}$$

Where e_n is the normal strain, original length of L_o to the deformed length of L [2].

All strain components of tensor apparent on an elemental volume in coordinates S_1, S_2 and S_3 as shown in equations 2.4.

$$\varepsilon_{ij} = \begin{bmatrix} \varepsilon_{11} & \varepsilon_{12} & \varepsilon_{13} \\ \varepsilon_{21} & \varepsilon_{22} & \varepsilon_{23} \\ \varepsilon_{31} & \varepsilon_{32} & \varepsilon_{33} \end{bmatrix} \tag{2.4}$$

Normal strain is two identical volumes, and shear strain is two mixed volumes [2].

2.4 Elasticity and Hooke's Law

The stress-strain relationships based on elasticity theory are used for measurement because stresses cannot be calculated by X-ray diffraction. Therefore, the stress is measured from the strains calculated from X-ray diffraction. The Hooke's law for strain is used when the deformation of a solid is within the elastic limit. Hooke's law for the stress–strain relations are given by equations 2.5 where C_{ijkl} are elastic stiffness coefficients [2].

$$\sigma_{ij} = C_{ijkl}\varepsilon_{kl} \tag{2.5}$$

Generalized Hooke's law stress–strain relations [2].

The uniaxial stresses state where only σ_{11} do not equal zero Hooke's law given by equations 2.6. Where E is a constant called the Young's modulus.

$$\varepsilon_{11} = \frac{\sigma_{11}}{E} \tag{2.6}$$

Uniaxial Hooke's law [2].

The equations 2.7 Hooke's law gives the shear stress and the shear strain. Where Shear modulus G, Young's modulus E, Poisson's ratio ν, and for a homogeneous isotropic materials [2].

$$2\varepsilon_{t} = \gamma = \frac{\tau}{G} \tag{2.7}$$

Hooke's law shear stress and the shear strain [2]

2.5 X-Ray Elasticity Constants and Anisotropy Factor

The strain measurement uses elastic constants S_1 and $1/2S_2$ for macroscopic X-ray diffraction, which is given by equations 2.8. A macroscopic level is isotropic residual stress is done by calculating the strain in crystal location to satisfy the Bragg condition.

$$\tfrac{1}{2}S_2 = (1+\nu)/E \quad \text{and} \quad S_1 = -\nu/E \tag{2.8}$$

Elasticity Constants [2].

The (A_{RX}) radiocrystallographic anisotropy element is a measure of the elastic anisotropy of the diffracting crystallites [2]. A_{RX} is between single crystal anisotropic element [9]. Some volumes of A_{RX} cubic materials are given in Table 2.1. Equation, 2.9 is another way to calculate A_{RX} .

Table 2.1: Some volumes of A_{RX} cubic materials [9].

Materials	A_{RX}
Body-centered cubic (bcc) Fe-base materials	1.49
Face-centered cubic (fcc) Fe-base materials	1.72
Face-centered cubic (fcc) Cu-base materials	1.09
Ni-base materials (fcc)	1.52
Al-base materials (fcc)	1.65

$$A_{RX} = \frac{\frac{1}{2}S_2^{\{h00\}}}{\frac{1}{2}S_2^{\{hhh\}}} \tag{2.9}$$

Calculate A_{RX} [2].

2.6 The $\sin^2 \psi$ Method

Stress measurements in polycrystalline materials can be done by the $\sin^2 \psi$ method, which can collect diffraction peaks of {hkl} by changing the ψ tilt angle orientation. Then, the slope of

$\varepsilon^{\{hkl\}}_{(\gamma,\omega,\psi,\phi)}$ plot can be measured by a linear least squares fitting and the stresses are calculated from the slope and the elastic constant [2]. Some different slopes of the $\sin^2 \psi$ Method is shown in Figure 2.4. First, the linear functions plot can be found if the principal (main) axes system is not tilted versus the sample's surface when σ_{13}, and σ_{23} are equal zero [8]. The elliptical functions plot can be obtained when the principal axes' system is tilted versus the sample's surface when σ_{13} and σ_{23} does not equal zero. The curved functions plot occurs in a strong stress gradient perpendicular to the surface [9]. In the end, the oscillating plot function is wavy lines that can appear of a texture material.

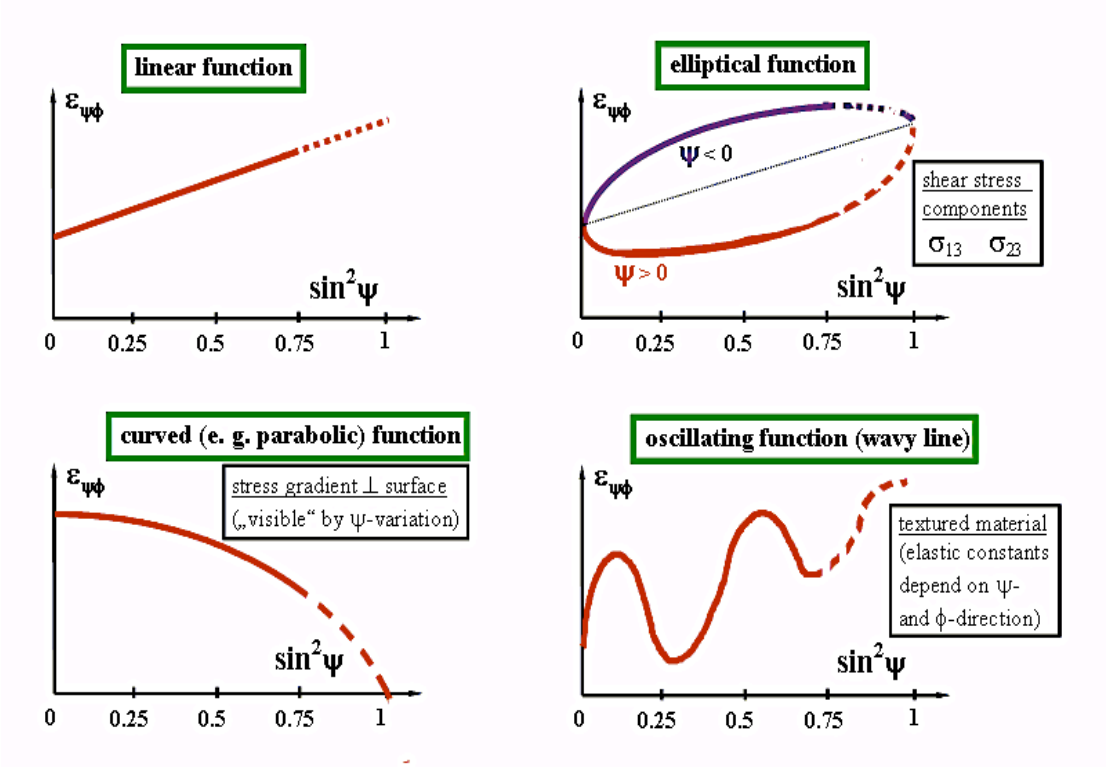

Figure 2:4: Different plots of $\sin^2 \psi$ method [8].

2.7 ψ Tilt and Goniometer

The ψ-tilt is an angle between the diffraction vector and the sample rotation (ψ, ω, ϕ) as shown in Figure 2.5 [2]. The calculation of a stress by $\sin^2 \psi$ method needs at least one ψ -tilt measurement; however, the measurement of a stress tensor contains two rotation axes to obtain the ψ-tilt and ϕ rotation. The ψ-tilt can be obtain by two modes which are iso-inclination and side-inclination.

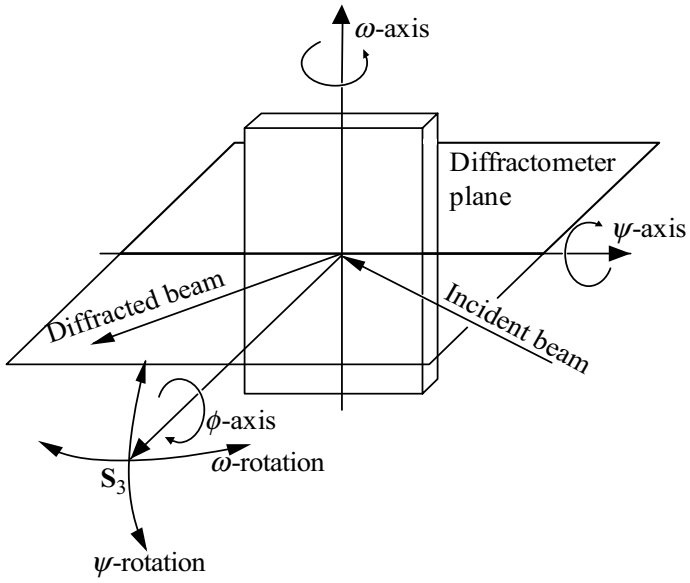

Figure 2:5: The ψ -tilt is achieved by rotation ω axis ϕrotation and ψrotation [2].

2.8 Fundamental Equation for Stress Measurement

There are two cones, one is the diffraction cone and other is the diffraction vector cone, as shown in Figure 2.6. The bright ring diffraction cones are without stress, as a result, the 2θ angles can

be constantan at γ angles. However, the dark rings are the cross sections of the distorted diffraction cones because of stresses. Therefore, 2θ enhances as a function of γ with sample orientation ω, ψ, and ϕ which is 2θ = 2θ(γ,ω,ψ, ϕ) [2]. This calculation is for the stress tensor. Also, the lattice plane family {hkl} diffraction cone has a diffraction vector cone as shown in Figure 2.6.

To measure a point on the diffraction ring P, is the analogous diffraction vector points to P_0. Therefore, the strain calculated by the 2θ shift at point P is $\varepsilon^{\{hkl\}}_{(\gamma,\omega,\psi,\phi)}$ as shown in equation strain 2.10 [2].

$$\varepsilon^{\{hkl\}}_{(\gamma,\omega,\psi,\phi)} = \ln\frac{d}{d_0} = \ln\frac{\sin\theta_0}{\sin\theta} = \ln\frac{\lambda}{2d_0\sin\theta} \tag{2.10}$$

Where d_0 and θ_0 are the stress-free values and d and θ are measured values from a point on the diffraction ring corresponding to (γ,ω, ψ, ϕ).

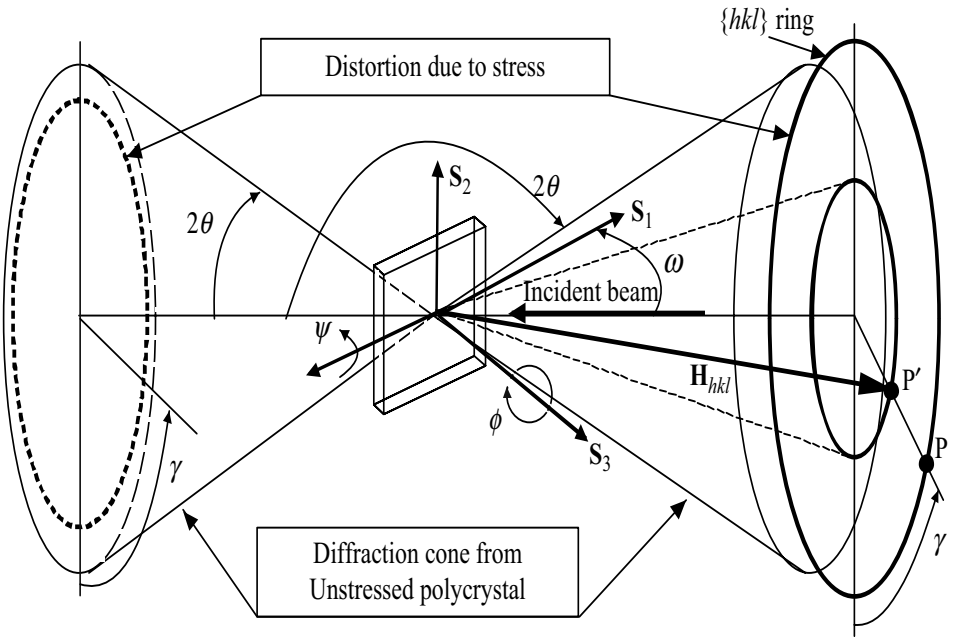

Figure 2:6: Stress Measurement [2].

For sample, the diffraction vector H and its unit vector h_L in the laboratory coordinates are given in Figure 2.7 based on Equation 2.11. The peak 2θ shifts were measured along the diffraction ring.

$$\boldsymbol{H} = \frac{\boldsymbol{s} - \boldsymbol{s}_0}{\lambda} = \frac{1}{\lambda}\begin{bmatrix} \cos 2\theta - 1 \\ -\sin 2\theta \sin\gamma \\ -\sin 2\theta \cos\gamma \end{bmatrix}$$
$$\boldsymbol{h}_{\mathrm{L}} = \frac{\boldsymbol{H}}{|\boldsymbol{H}|} = \begin{bmatrix} h_x \\ h_y \\ h_z \end{bmatrix} = \begin{bmatrix} -\sin\theta \\ -\cos\theta \sin\gamma \\ -\cos\theta \cos\gamma \end{bmatrix} \qquad (2.11)$$

Where Diffraction vector is H and its unit vector h_L [10].

The residual stress was measured by the relationship between the stress tensor and the diffraction cone distortion [9]. The diffraction intensity distributions in both 2θ and γ directions were measured, along with the unit diffraction vector to be found with respect to the sample coordinates.

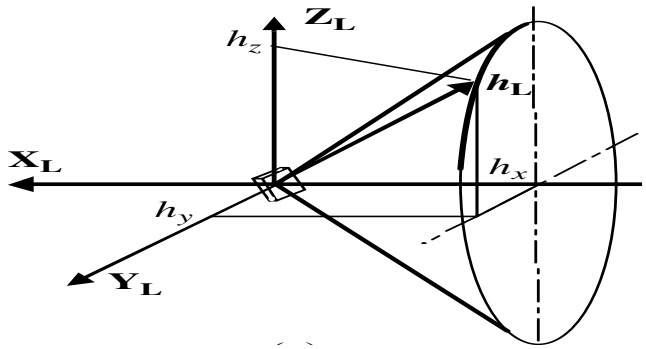

Figure 2:7: H_L unit vector of diffraction [9].

Equation 2.12 gives the transformation $h_s=A*h_L$, where the unit vector is h_s of the diffraction vector shows the sample geometrics S_1, S_2, and S_3 as shown in Figure 2.8. The diffraction vector is h_L can be calculated from the unit vector in coordinates.

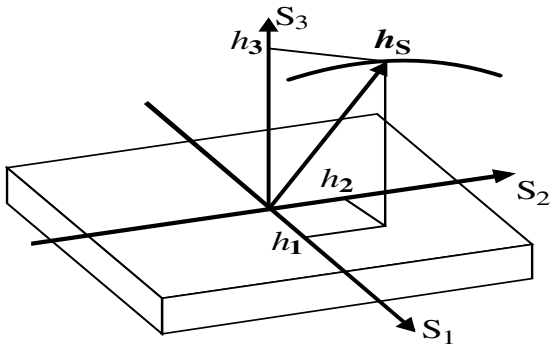

Figure 2:8: Coordinates S_1, S_2, and S_3 with h_s [10].

$$\begin{bmatrix} h_1 \\ h_2 \\ h_3 \end{bmatrix} = \begin{bmatrix} -\sin\omega\sin\psi\sin\phi - \cos\omega\cos\phi & \cos\omega\sin\psi\sin\phi - \sin\omega\cos\phi & -\cos\psi\sin\phi \\ \sin\omega\sin\psi\cos\phi - \cos\omega\sin\phi & -\cos\omega\sin\psi\cos\phi - \sin\omega\sin\phi & \cos\psi\cos\phi \\ -\sin\omega\cos\psi & \cos\omega\cos\psi & \sin\psi \end{bmatrix} \begin{bmatrix} -\sin\theta \\ -\cos\theta\sin\gamma \\ -\cos\theta\cos\gamma \end{bmatrix} \quad (2.12)$$

Transformation $h_s = A * h_L$.

2.9 True Stress-Free Lattice d-Spacing

There is an error that can occur from the calculation. For instance, in the two-dimensional stress, σ_{33} are zero for the biaxial and biaxial with shear tensor with an estimate of d_0 or 2θ, which cause an error. Therefor, any error in d_0 or 2θ donated only to a pseudo-hydrostatic term σ_{ph}. The calculation of stresses change depends on the input d_0 or 2θ values [2]. Pseudo-hydrostatic term can be proven by Almen strip [2]. The Almen strip is a thin strip of metal sample used to quantify the intensity of a shot peening process [2]. The strip is shot peened in a shot peening chamber. In addition, when d_0 is the initial input, then the true d_0 or 2θ can be calculated from σ_{ph} by equations 2.13.

$$d_0 = d_0' \exp\left(\frac{1-2\nu}{E}\sigma_{ph}\right) \quad (2.13)$$

$$\theta_0 = \arcsin\left[\sin\theta_0' \exp\left(\frac{2\nu-1}{E}\sigma_{ph}\right)\right]$$

True Stress-Free Lattice d-Spacing to Pseudo-hydrostatic term [2].

2.10 Data Integration and Peak Evaluation

The data integration and peak is a means of estimating data points along deformed diffraction rings at several specimen orientations. The data integration for residual stress evaluation is γ-integration over several defined segments. As a result, the diffraction ring indicates the corresponding segments, as shown in Figure 2.9. An analytic function can fit the data points to a model profile. Next, evaluating the data points can determine the peak position, with one data point on the diffraction ring produced from each segment. The γ-integration of the segments produces diffraction profiles. Then, the 2θ value is determined from each of the profiles [2]. According to the condition of the data frame, the segment size (Δγ) and the number of segments is chosen. A larger (Δγ) is better due to more counts integrated. The 2θ shift in the segment is averaged. However, it is important to select the appropriate segment size the frames collect.

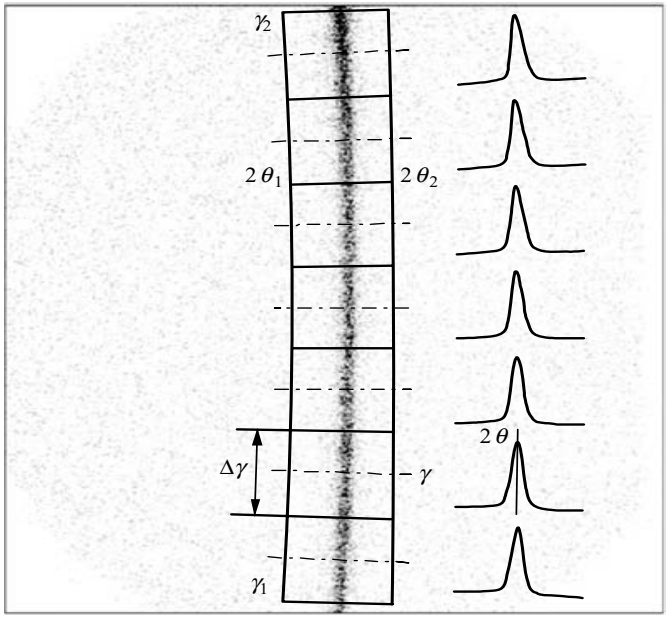

Figure 2:9 Data integration for stress measurement [2].

In addition, the corrections on the integrated rings are performed during or before the peaks calculation. Absorption correction removes the effect of the diffraction geometry and the irradiated area on the calculated intensity distribution. The absorption depends on the incident angle to the specimen and the returned angle from the specimen. The returned angle is a function of γ on each frame. The polarization influence is a function of γ. Consequently, the correction for absorption and polarization should be applied to the frame before integration. Also, background, $K\alpha_2$, and smoothing can apply to each frame. The background work calculates data points around the thin curve and eliminates scattered intensity that does not contribute to the diffraction profile. Smooth eliminates effect of counting statistics on the result of Background and $K\alpha_2$. There are the peak fitted position evaluated to a Gaussian, Cauchy (or Lorentz), Voigt, pseudo-Voigt, and Pearson VII [2]. One of these fitting is the Pearson VII, which is fitted to a broad range of line shapes a shown in Figure 2.10, with equation 2 .14.

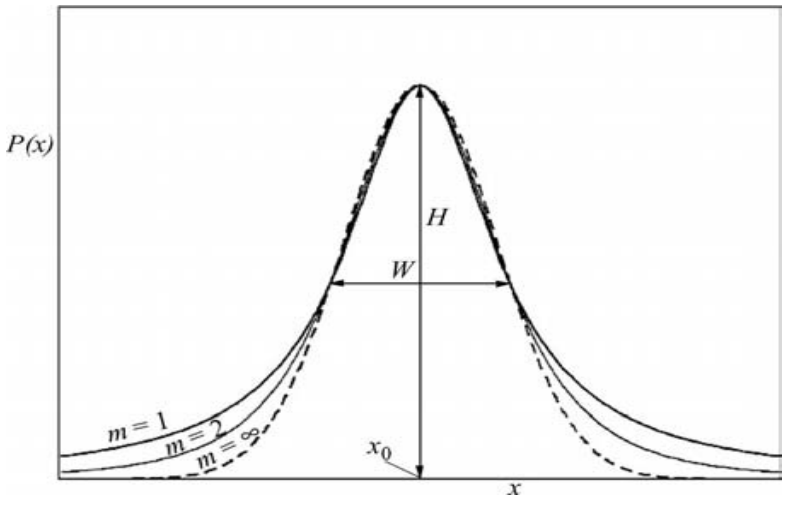

Figure 2:10:Pearson VII [2].

$$P(x) = H\left[1 + 4\left(2^{1/m} - 1\right)\left(\frac{x - x_0}{W}\right)^2\right]^{-m} \quad (2.14)$$

Where W is the FWHM (full width half maximum) of the lines, M is a shape parameter, and H is a scaling factor that determines the height of the peak [2].

2.11 Conventional Method and two-dimensional diffraction Method

Stress measurement by X-ray diffraction is founded by the strain measurements in several or a single specimen orientation. Each strain calculation is estimated from the average d-spacing of lattice planes {hkl} over several grains. The diffraction collected by (a) a point detector or (b) an area detector is shown in Figure 2.11 [2]. The conventional method is to collect the data point by a point detector, which measures only a few crystallite data points by the incident beam, hits the specimen and diffracted beam collected by the point detector. However, a two-dimensional diffraction system collects the diffraction rings of γ angles by area detector. Consequently, two-dimensional diffraction can collect more crystallites. In addition, a larger γ angle is better due to collection from more crystallites.

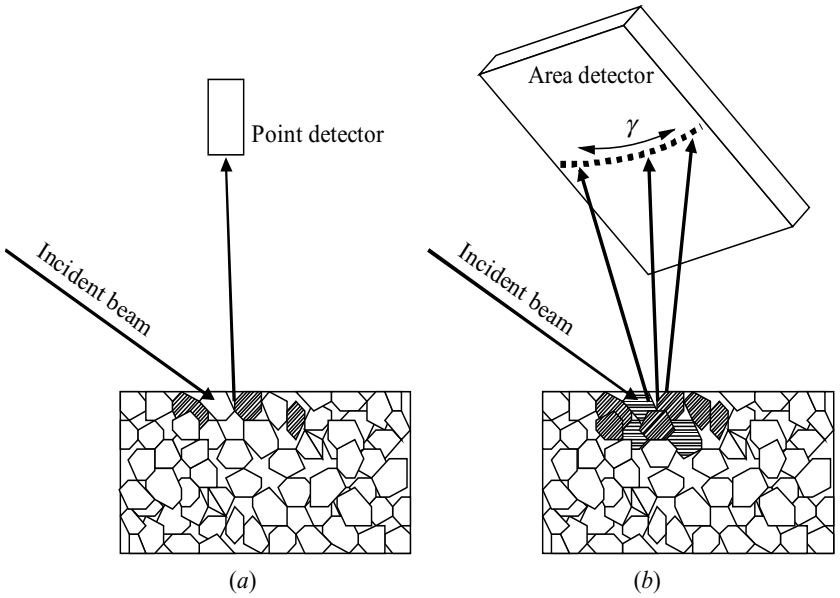

Figure 2:11: Diffraction collected by (a) a point detector or (b) an area detector [2].

Chapter 3

LEPTOS

3.1 LEPTOS STRESS

LEPTOS is software designed to display, fit, and analyze data collected by X-ray diffraction. In addition, LEPTOS uses the dynamical theory to simulate X-ray diffraction in various geometries to calculate the data [8] it also has capabilities for analysis of wafer area mapping measurements [8]. All the data analysis procedures can be managed by LEPTOS in fully automated script mode. It gives an advantage of building a convenient and logical interface for data analysis. LEPTOS was used in analysis phase identification, thin film, texture analysis, stress measurement and others.

3.2 Residual Stress by LEPTOS software

LEPTOS STRESS calculates the residual stress measurements with 1, and 2-dimensional detectors. Certain parameters should be considered such as material, Young's modulus E, and Poisson ratio. The Miller indices plane hkl must be chosen for Bragg reflection. The wavelength of radiation anode element such as Ag, Mo, Co and others are chosen depending on the sample material. The stress-free 2θ in the vicinity of must be selected to represent double the Bragg angle for the unstressed lattice plane. The X-ray elastic constants are calculated from S_1 and $1/2S_2$. The measure of the elastic anisotropy of a cubic material is A_{RX} must be determined. However, 1D curve and 2D stress frame is shown in Figure 3.1

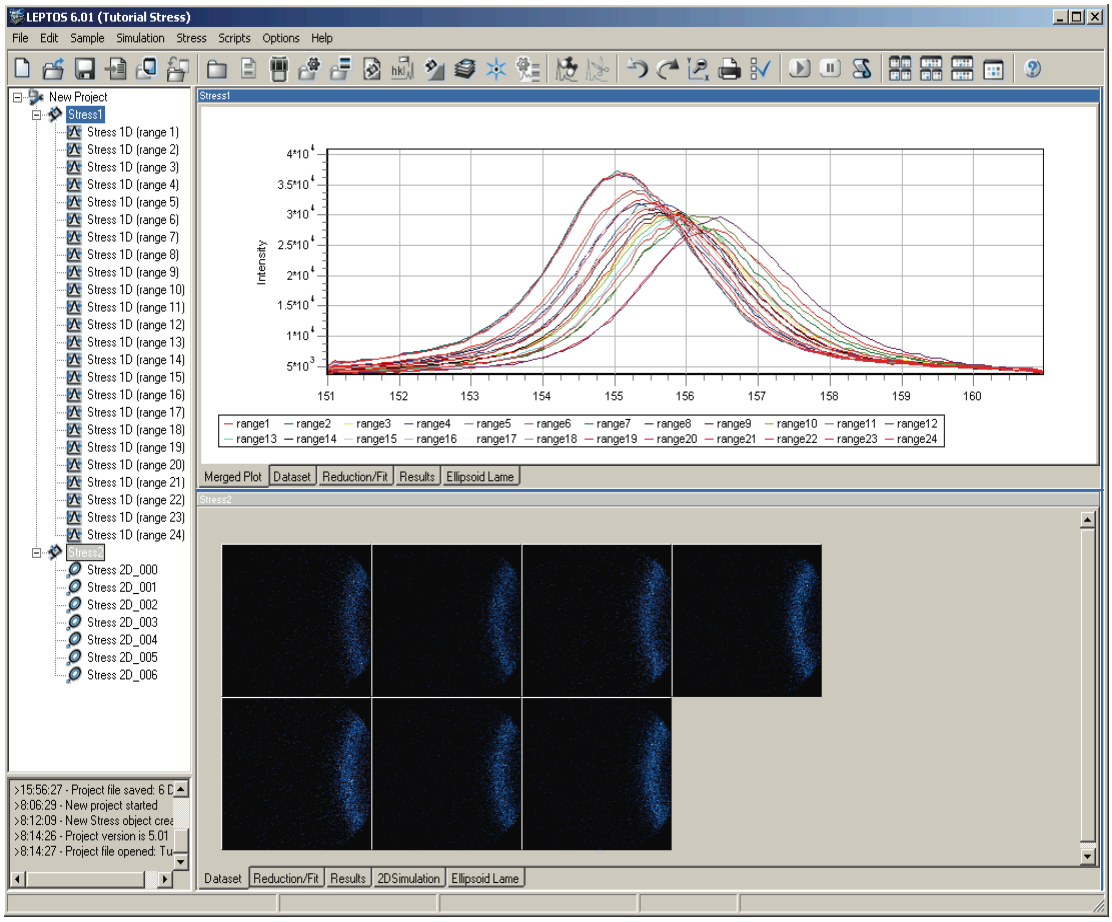

Figure 3:1: 1D and 2D Stress curve in LEPTOS [8].

3.3 Corrections and Peak Evaluation Methods

Corrections of both 1D and 2D stress measurements contain Absorption, Background, Polarisation, $K\alpha_2$, and Smoothing corrections applied to each measured curve in a stress object and may be selected if needed as shown in Figure 3.2. The peak evaluation of both 1D and 2D Stress LEPTOS can be selected as shown in Figure 3.3.

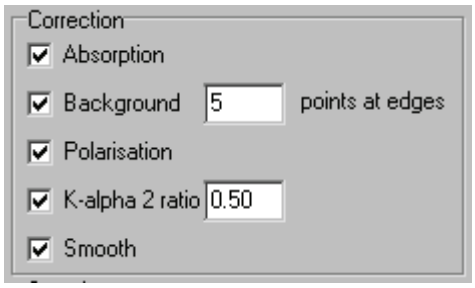

Figure 3:2:Corrections [8].

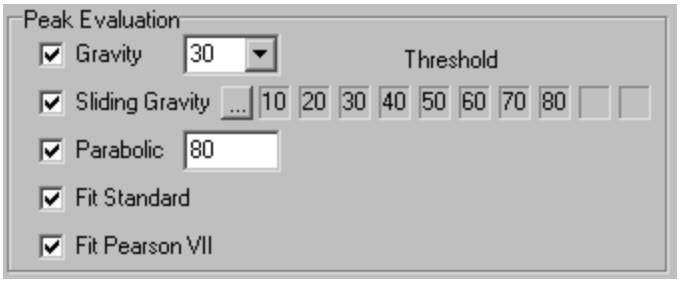

Figure 3:3: Peak Evaluation [8].

3.4 Two-dimension stress

The two-dimensional stress means evaluation of data consisting of the set of frames. After the two dimensional detector collects the data points into to dimensional data frames or maps into stress object. Then, LEPTOS is ready for evaluation of the sample stress status as shown in Figure 3.4.

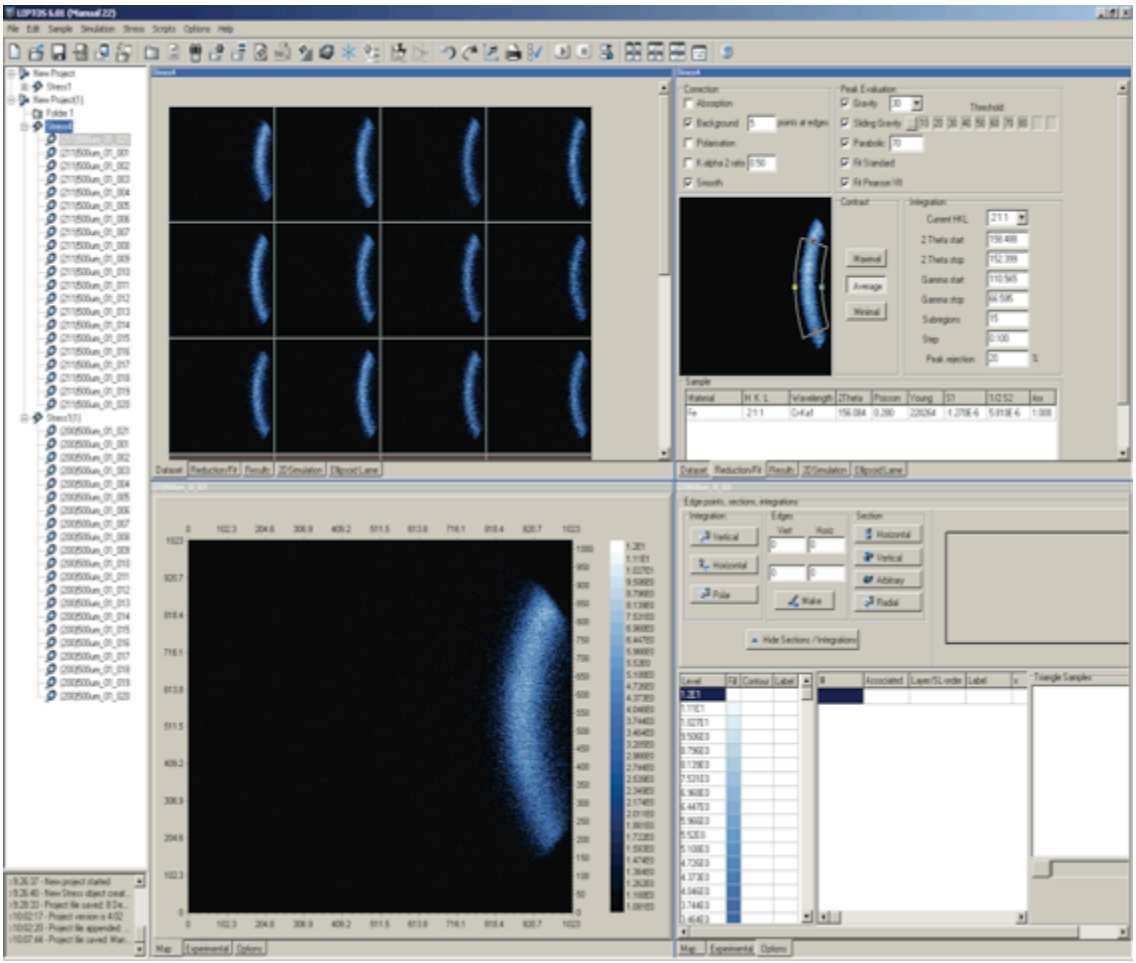

Figure 3:4: Two-dimension stresses [8].

The Integration sets the wire frame change the integration area based on the corresponding values of angles 2Theta start, 2Theta stop, Gamma start, and Gamma stop as shown in Figure 3.5 and Figure 3.6.

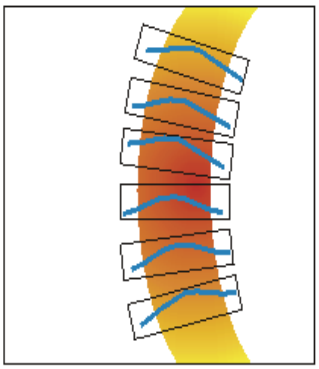

Figure 3:5: Integration sets on the wire frame [8].

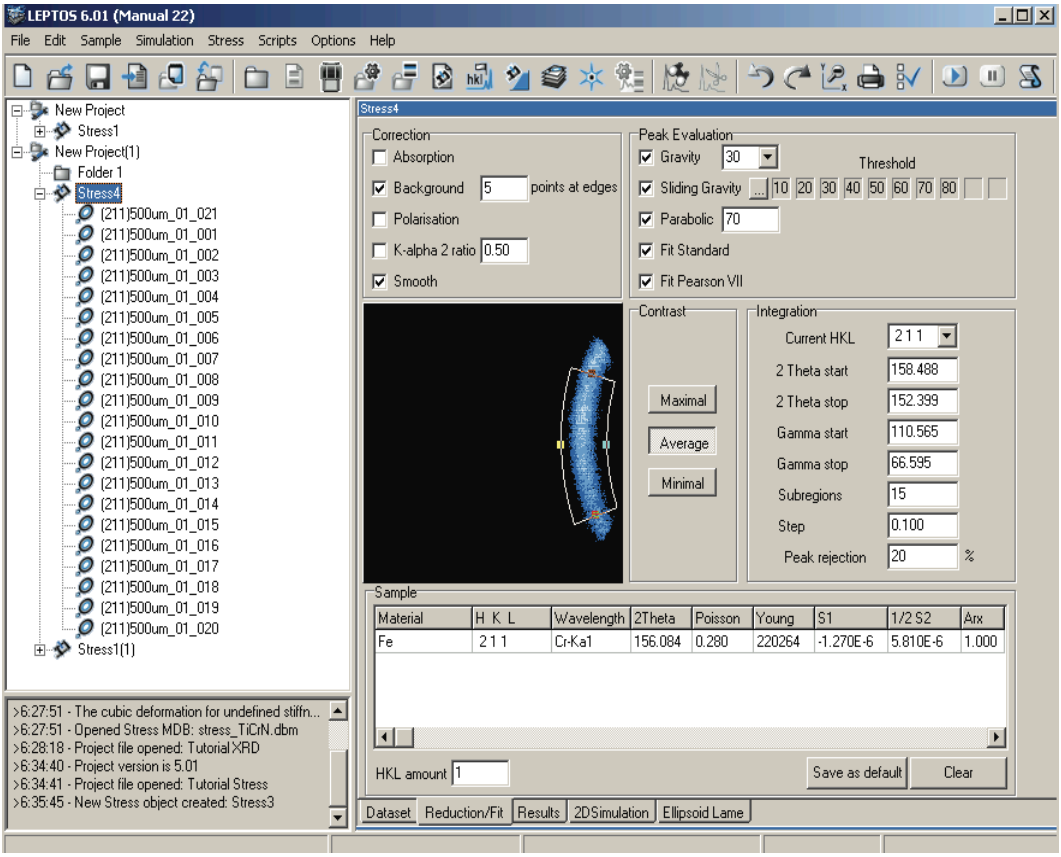

Figure 3:6: Integration sets on the wire frame [8]

3.5 Stress tensor

The stress tensor can be selected based on the type of measurement as shown in Figure 3.7. The blue line is an unwrapped Debye ring calculated with the respect to the calculated stress tensor, and the shadowed area designates the left and the right limits of the γ angle scale, measured by the detector. The sliders allow variation of the goniometer angles and detector distance to estimate the segment of the measured Debye ring [8].

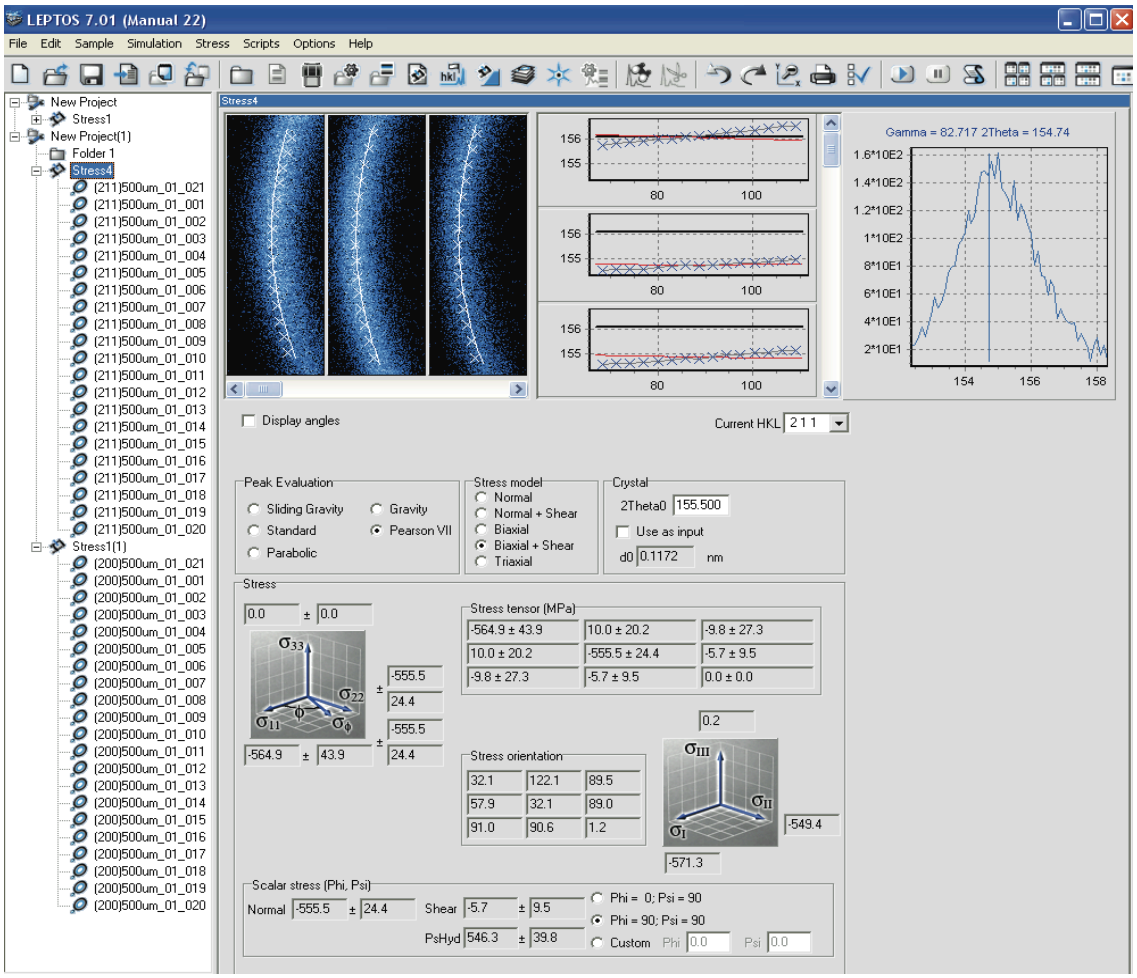

Figure 3:7: Stress tensor [8]

Chapter 4

Finite Element Analysis

4.1 Introduction

Finite Element Analysis (FEM) is a popular method used in technology due to its ability to model and simulate various engineering and mathematical physics problems. Finite Element Analysis obtains approximate solutions of many problems such as heat transfer, fluid flow, physical displacement, and temperature. In finite element analysis, there are many equations for various types and dimensions, which can be one- dimensional, two-dimensional and three-dimensional structures. In addition, theses applications are trusses element, beams element, shell element, and others as shown in Figure 4.1. FEM goal is to reduce cost of the structure and the weight. There are various FEM software which are used to simulate various problems such as Abaqus, Ansa, Comsol and others. In this thesis I focus on three-dimensional solid element by Abaqus software.

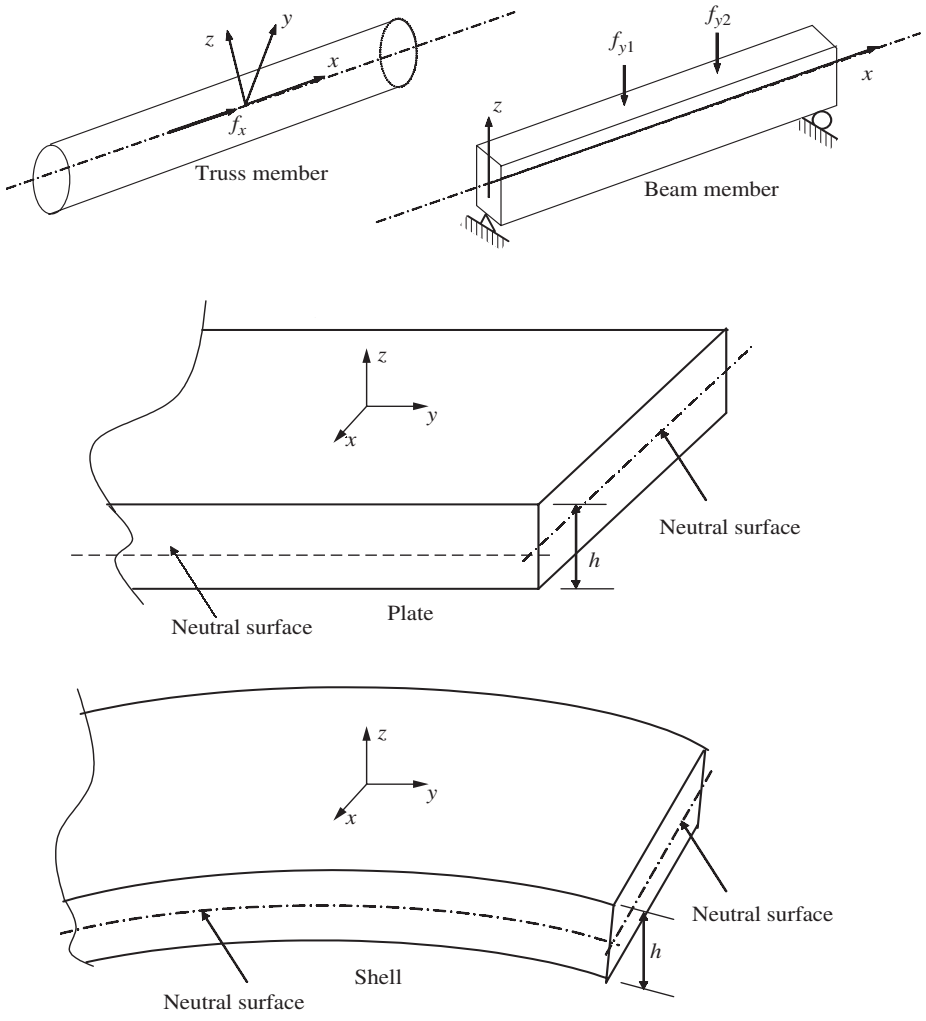

Figure 4:1: Structural components of FEM [11]

4.2 Three-dimensional solid

In a three-dimensional (3D) elastic solid, there is a volume V and a surface S, as shown in Figure 4.2. The shell of the solid is separated into two kinds of surfaces one surfaces is S_f, which the external forces are set and other surface is S_d, which the displacements are set. In addition, the

external load can apply by surface force f_s and body force f_b in any direction in the volume of the solid. The stress components can be at any point in on the surface of cubic volume as shown in Figure 4.3. The stress components can be divided into normal stress and shearing stress.

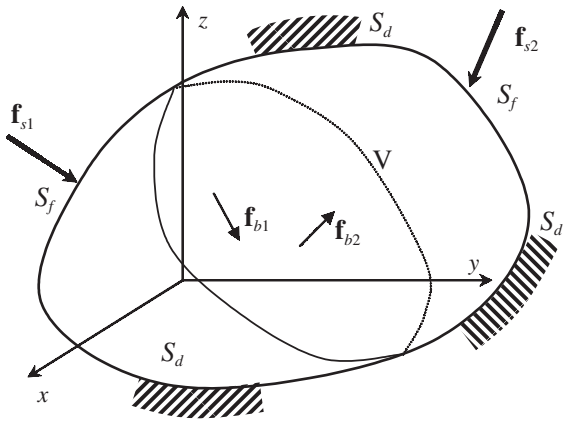

Figure 4:2:Three-dimensional elastic solid [11].

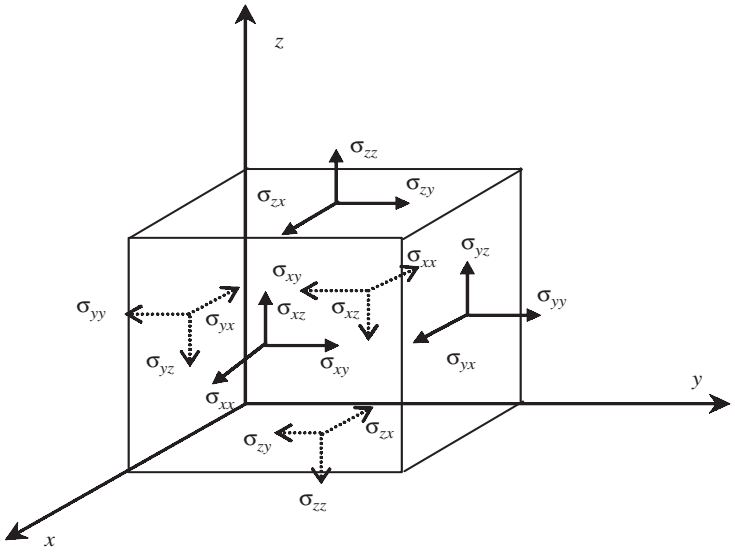

Figure 4:3:The stress components of cubic volume [11].

The relationship between the stress and strain is the constitutive equation, which is the Hooke' s law term. For anisotropic materials is given by Equation 4.1 in the following matrix.

$$\sigma = c\varepsilon \tag{4.1}$$

$$\begin{Bmatrix} \sigma_{xx} \\ \sigma_{yy} \\ \sigma_{zz} \\ \sigma_{yz} \\ \sigma_{xz} \\ \sigma_{xy} \end{Bmatrix} = \begin{bmatrix} c_{11} & c_{12} & c_{13} & c_{14} & c_{15} & c_{16} \\ & c_{22} & c_{23} & c_{24} & c_{25} & c_{26} \\ & & c_{33} & c_{34} & c_{35} & c_{36} \\ & & & c_{44} & c_{45} & c_{46} \\ & sy. & & & c_{55} & c_{56} \\ & & & & & c_{66} \end{bmatrix} \begin{Bmatrix} \varepsilon_{xx} \\ \varepsilon_{yy} \\ \varepsilon_{zz} \\ \varepsilon_{yz} \\ \varepsilon_{xz} \\ \varepsilon_{xy} \end{Bmatrix}$$

The constitutive equation [11].

Where **c** is a matrix of material constants as shown below [11]

$$c_{11} = \frac{E(1-\nu)}{(1-2\nu)(1+\nu)}; \quad c_{12} = \frac{E\nu}{(1-2\nu)(1+\nu)}; \quad \frac{c_{11}-c_{12}}{2} = G$$

Where are E, Young's modulus, ν Poisson's ratio and G shear modulus. The relationship between these three constants is given below.

$$G = \frac{E}{2(1+\nu)}$$

4.3 Residual stress analysis by Abaqus

To predicate residual stress finite element analysis software package is needed to estimate residual stresses. In this case, Abaqus software was used to estimate residual stresses. There are some methods to obtain residual stress such as by Quasi-Static Analysis, initial conditions, Moldflow interface files, or loading unloading step. Each of these methods is used for different analysis. For instance, Moldflow with Abaqus is used to obtain the residual stress in plastic flow of a material. However, in this research, loading and unloading step is used. There are steps in module, which provides a suitable way to change the loading and boundary conditions of the model. The residual stress occurs after plastic deformation. Therefore, the residual stress can obtain by applying unloading step in module to obtain residual stresses. However, in this research, elastic- plastic deformation was investigation to obtain the residual stresses direction.

Chapter 5

Results and Discussion

5.1 Introduction

In 2000, Almer, Cohen, and Moran investigated the effects of residual macro stresses and micro stresses on fatigue crack initiation by using X-ray diffraction and finite element analysis to predict fatigue crack initiation in the presence of residual stresses [14]. These researchers identified residual stresses in notched 1080 steel samples. Residual stresses were investigated by press-fitting operations and pre-straining, and crack initiation was observed through high-cycle fatigue analysis. Internal stress and strain behaviour was found in the vicinity of the initiation sites by using finite element analysis. Almer, Cohen, and Moran created micro beam X-ray diffraction to measure residual macro stresses in different phases of 1080 steel alloy, and found that the macro stresses were relaxed, thereby affecting the beginning of cracking. They claimed that the micro stresses would disappear during fatigue test [14]. The researchers used one-dimensional X-ray diffraction as well as a multi-purpose finite element program written by Prof. R. L. Taylo for mounding test [14].

Since then, further research analysis of residual stress has been completed on stamped valves by X-ray diffraction and finite elements method [15]. In 2006, Martins, Cardoso, Fraymann, and Button analyzed residual stresses in stamped valves by X-ray diffraction and finite element method. They used a sin2 ψ method one-dimensional X-ray diffraction to calculate the residual stresses in small areas of the stamped valves. The researchers mounded some parts of the stamped valves by MSC Superform version 2004 code. Results were then compared with

simulation. In addition, fatigue tests were completed which analyzed endurance bench by applying alternate reverse bending on dynamical valves [15]. Finally, Martins et al. claimed that the residual stresses resulting from the fatigue tests proved the validity with finite element analysis.

In 2010, Robinson, Tanner, Truman, and Wimpory investigated residual stress using Neutron diffraction testing with FEM Abaqus software package to measure and predict machining induced redistribution of residual stress in the Aluminium alloy 7449 [16]. A heat treatment was performed with cold water immersion quenching before precipitation hardening, and high magnitude residual stresses were calculated in the material of two blocks. One block was milling to thickness while the other block measured without external effect. The researchers used non-destructive testing Neutron diffraction to measure the residual stress and compared both results for both blocks. Arising distortions were also calculated using a coordinate measuring machine [16]. In addition, a moulding was completed using finite element analysis Abaqus to compare the result with the experiment Neutron diffraction testing. Robinson et al. claimed that the results generally agree with each method [16].

In 2004, Anderoglu used one-dimensional X-ray diffraction to analyze residual stresses [17]. SS316 stainless steel samples were investigated along with residual stresses analysis using Bruker-AXS GADDS 2D Powder and Single-crystal X-Ray Diffractometer. Eight samples of residual stresses were analyzed and results were compared in different angle orientation with a biaxial model being used to obtain the residual stress. The researcher claimed that the change angle orientation gives different residual stresses analysis [17].

In 2012 Yuting and Junyi did simulations of residual stress induced by waterjet peening using Abaqus [18]. Two different methods were used to calculate residual stresses with a quasi-static analysis and transient dynamic analysis using 2D and 3D modules. The researchers stated that residual stresses differed between each loading and unloading step. The results in quasi-static analysis and transient dynamic analysis differed between two- and three-dimensional [18].

Overall, most research calculated residual stresses by using different non-distractive testing. However, thin plates are common in engineering applications. This thesis analyzes residual stresses in AISI 1020 steel alloy cold rolled manufacture processing plates. Two identical thin circular plates are used in this experiment; one of which is statically loaded. The other plate is used as a control specimen. Residual stresses in the plates are measured using two-dimensional X-ray diffraction and the measurements are compared to those obtained using finite element analysis. It was found that experimentally measured residual stress occurred due to manufacture processing. Also, modules A and B showed the external effect of applying not enough to reach the plastic region to deform specimen 2 and obtain residual stress results distribution. The two specimens were thin annular desks with dimension of: 0.79 mm thickness, 38 mm outside diameter, and 25 mm inside diameter. One plate was loaded with a static compressive load of 26.689 KN, referred to as specimen 2 as shown in Figure5.1. The mechanical and physical material properties of AISI 1020 steel alloy cold rolled plates are given in table 5.1 [19].

Table 5.1: Material properties of AISI 1020 steel alloy cold rolled plates [19].

Physical Properties	Metric	English	Comments
Density	7.87 g/cc	0.284 lb/in³	

Mechanical Properties	Metric	English	Comments
Hardness, Brinell	121	121	
Hardness, Knoop	140	140	Converted from Brinell hardness.
Hardness, Rockwell B	68	68	Converted from Brinell hardness.
Hardness, Vickers	126	126	Converted from Brinell hardness.
Tensile Strength, Ultimate	420 MPa	60900 psi	
Tensile Strength, Yield	350 MPa	50800 psi	
Elongation at Break	15 %	15 %	In 50 mm
Reduction of Area	40 %	40 %	
Modulus of Elasticity	205 GPa	29700 ksi	Typical for steel
Bulk Modulus	140 GPa	20300 ksi	Typical for steel
Poissons Ratio	0.29	0.29	
Machinability	65 %	65 %	Based on AISI 1212 steel. as 100% machinability
Shear Modulus	80.0 GPa	11600 ksi	Typical for steel

Figure 5:1: Compressive machine.

5.2 Bruker LEPTOS software

The residual stresses calculation on the two, thin, circular plates was analyzed with Bruker LEPTOS software [8]. In the experiment, the input material is iron (Fe) with a Young's modulus of E = 205 GPa and a Poisson ratio of $\nu = 0.29$. The Miller indices plane is hkl (211) for Bragg reflection. Co-Kα_2 radiation was used to avoid Fe fluorescence. The stress-free 2θ in the vicinity of 99.6° was double the Bragg angle for the unstressed lattice plane. The X-ray elastic constants of steel alloy 1020 were calculated -1.271E -6 for S_1 and 5.811E-6 for$1/2S_2$ using equation.2.8 [2]. The measure of the elastic anisotropy of a cubic material is 1 A_{RX}. The biaxial model was chosen to calculate residual stresses, as given by equation 2.2 [2].

5.3 Frame preparation

After data collection, the residual stresses were calculated by using the VÅNTEC-500 detector as shown in Figure 5.2. The frames required preparation prior to final calculation. Corrections were applied to each measured curve in stress, if needed. In the experiment, the background work calculated five data points around the curve and eliminated the scattered intensity that does not contribute to the diffraction profile. Absorption is one example because it eliminates the diffraction intensity, as is polarization, because it affects the calculation of the positions of absolute peaks. The Kα_2 line 0.5 was used for the intensity ratio. Smoothing was used to eliminate the effect of counting statistics on the results of the background and Kα_2**.**The peak position was evaluated using Pearson VII, which is used to fit a broad range of line shapes as shown in Figure 2.10 and equation 2.16.

Figure 5:2: VÅNTEC-500 detector [10].

5.4 Experimental test

The thin, solid lines shown in Figures 5.3 to 5.8 represent data integration over diffraction frames. The diffraction solid line ring was measured from the lattice plane family (211). The total integration region was given by 2θ, began at 101.5° and ended at 97.5°, and γ began at -73.9°and ended at -106.2° for stress analysis. Δγ was 10°. Figures 5.3 to 5.8 show examples of different frame samples with the same orientation: (a) illustrates the data collection scheme for stress data points collected at ω omega 50° constant, 4ψ psi angles at (15, 40, 65, 80), and 13 ϕ phi at (65, 110, 155, 200, 80, 103, 126, 172, 195, 80, 98, 116, 134). Both samples had a pseudo-hydrostatic term σ_{ph} standard error of 0.0±18.8, and the final d_0 = 0.1171 nm and 2θ was 99.64°. For the first sample, the residual stresses were σ_{11} = 240 ± 24 MPa and σ_{22} = 252.5±21.224 MPa. Therefore, these results indicate a slightly higher standard error with a principal stress tensor of

σ_I = 263.224 MPa and σ_{II} = 229.324 MPa. For the second loaded sample, the residual stresses were σ_{11}= 285 ± 20 MPa and σ_{22} = 219.3±20.424 MPa. Therefore, these results indicate a significantly higher standard error with principal stress tensor of σ_I = 285.424 MPa and σ_{II} = 218.924 MPa.

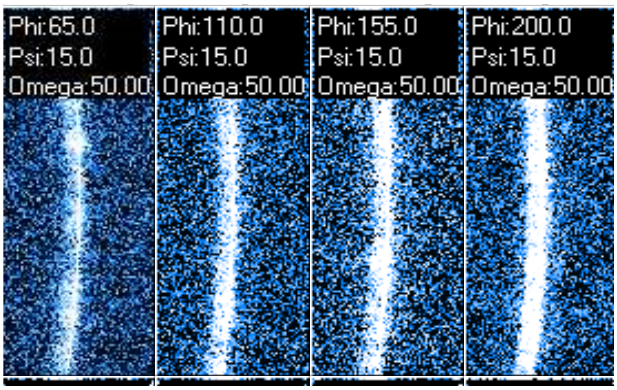

Figure 5:3: Frames orientation (ω 50, ψ15, ϕ 65,110,155, 200) for specimen 1.

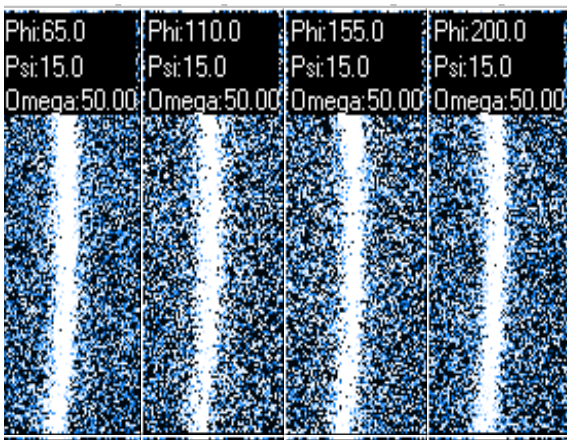

Figure 5:4: Frames orientation (ω 50, ψ 15, ϕ 65,110,155,200) for specimen 2.

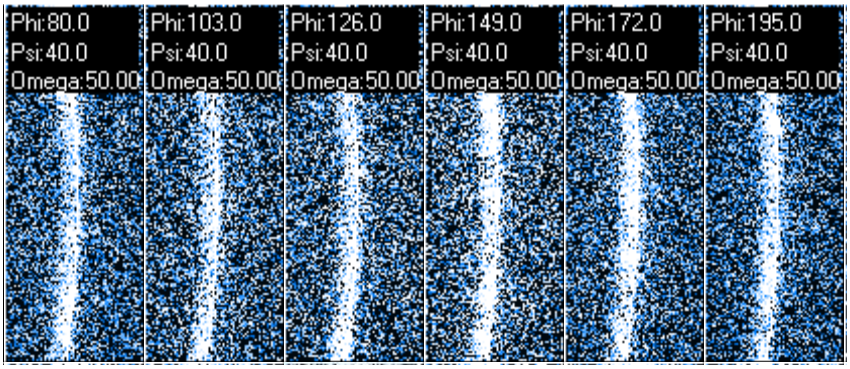

Figure 5:5: Frames orientation (ω 50, ψ 40, ϕ 80,103,126,149,172,195) for specimen 1.

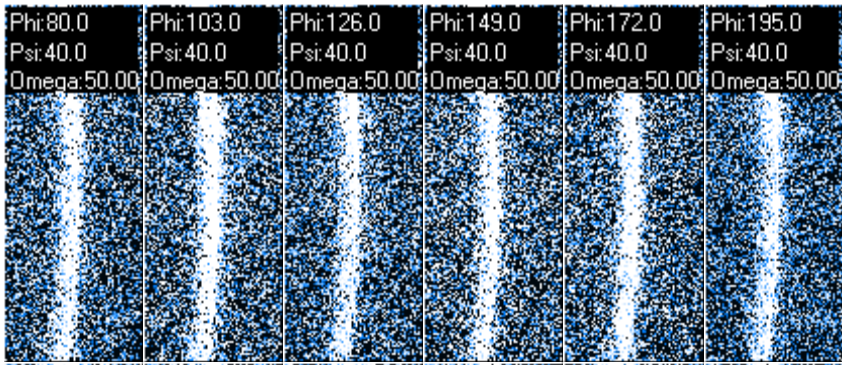

Figure 5:6: Frames orientation (ω 50, ψ 40, ϕ 80,103,126,149,172,195) for specimen 2.

As a result, the thin solid lines represent data integration over a diffraction frame shown in specimen 2, and the residual stress distribution is higher than in specimen 1. However, not all frames can have data integration calculated in the experiment, some frames had insufficient data points as show in Figure 5.7 and Figure 5.8. These frames orientation did not satisfy Bragg's law. This experiments were done at McMaster University in chemistry department X-ray lab, and more information about the experiment is provided in Appendix A and B.

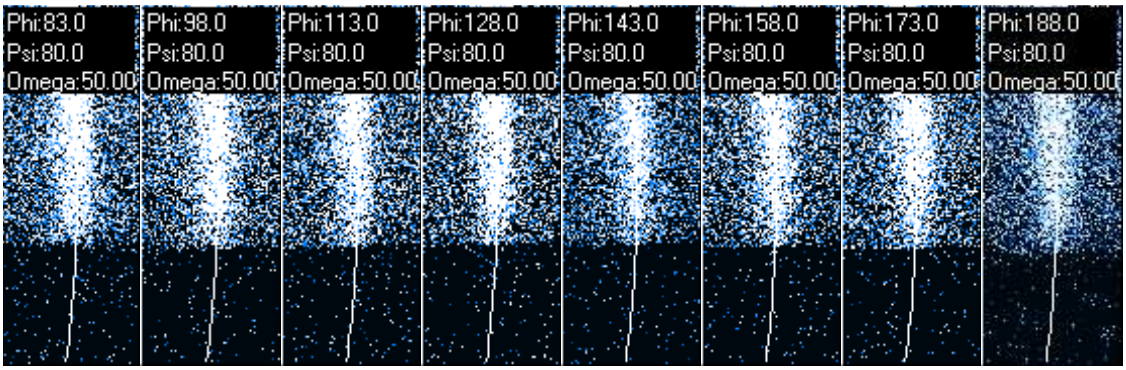

Figure 5:7: Frames orientation (ω 50, ψ 80, ϕ 83,98,113,128,143,158,173,188) for specimen 1.

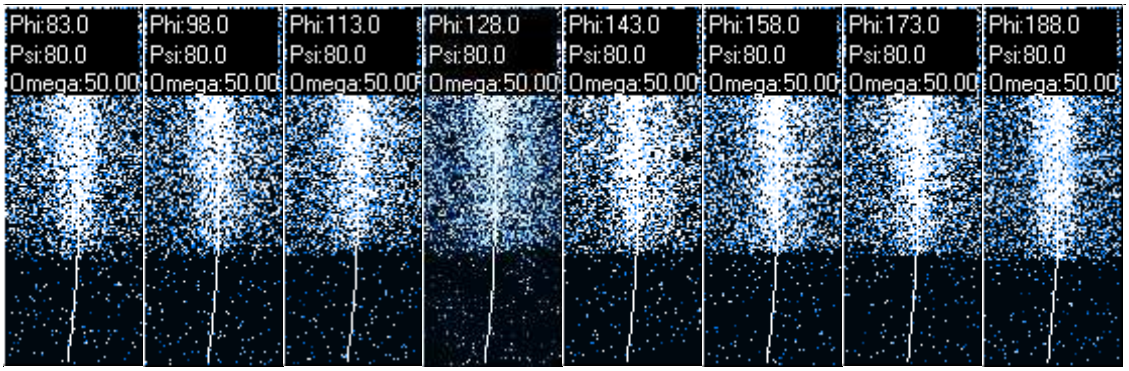

Figure 5:8: Frames orientation (ω 50, ψ 80, ϕ 83,98,113,128,143,158,173,188) for specimen 2.

5.5 The finite element analysis

Finite element analysis code Abaqus, version 6.12 [12], was used to predict the residual stress distribution in specimen # 2. Modules A and B proved the amount of pressure which was needed to get residual stress distribution. A three-dimensional element model of the circular steel plate was modeled using A three-dimensional solid elements. Material response was assumed to

be isotropic and to follow elastic-plastic deformation and undergo strain hardening during plastic deformation. The elastic material properties were set to Young's modulus of E = 205 GPa and a Poisson ratio ν = 0.29. The plastic stress-strain relationship was described using four points on the curve adopted as shown in Figure 5.9 [12]. True stress and true strain volume are given in table 5.1. The mesh of the plate was made of hex 3D solid elements (type C3D8R) as shown Figure 5.10. For module A, a uniform compressive pressure of 41.5 MPa was applied on the top surface of the plate. However, for module B, a uniform compressive pressure of 300 MPa was applied on the top surface of the plate. For both modules, displacement was constrained to zero in Z directions of the bottom plate as shown in plate Figure 5.11. The model followed Abaqus standard procedure to predict residual stress.

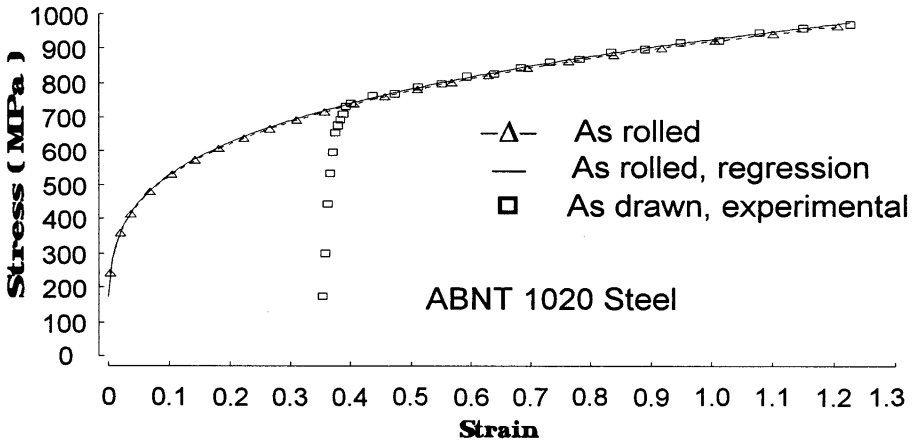

Figure 5:9: The plastic stress-strain relationship curve [20].

Table 5.2: The plastic stress- strain volume [12].

Yield Stress (MPa)	Plastic Strain
250	0.0
350	0.1
550	0.2
600	0.3
700	0.4
750	0.5
800	0.6

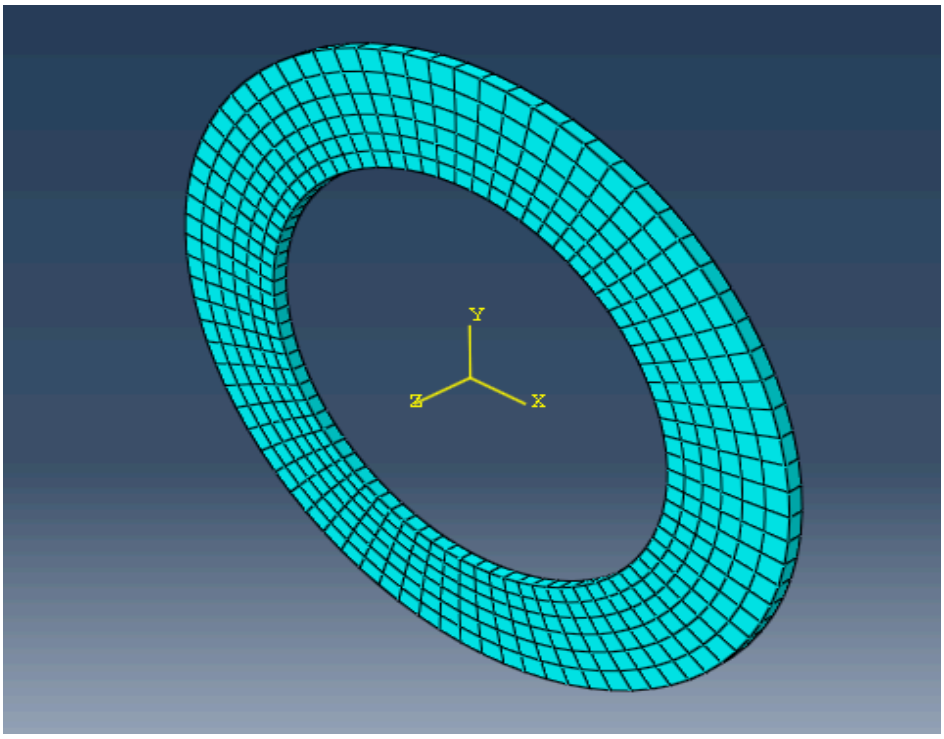

Figure 5:10:Mesh elements.

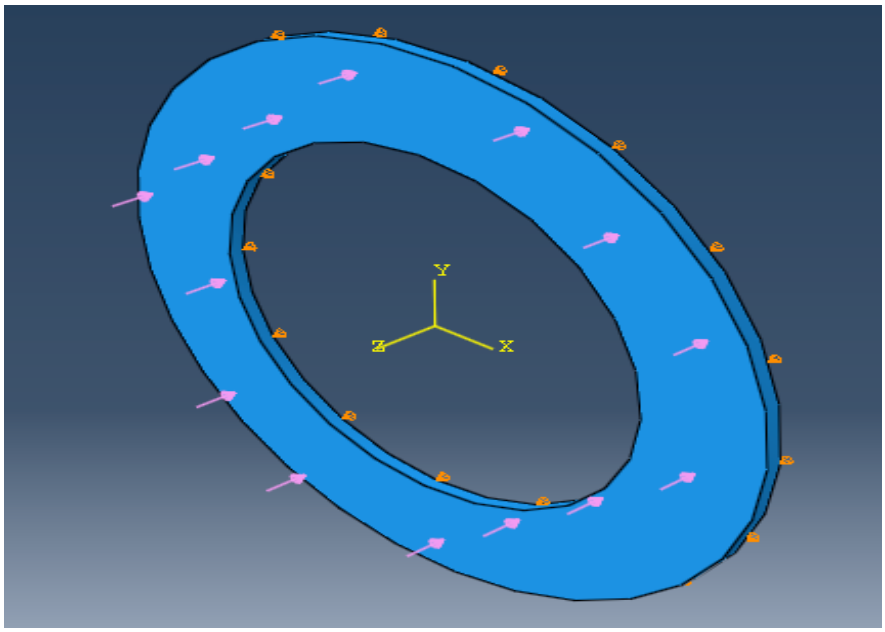

Figure 5:11: Uniform pressures with boundary condition.

5.6 Finite Element Analysis Results

After the specimen was loaded and the load removed, the residual stresses were determined. For module A, a uniform compressive pressure of 41.5 MPa was not enough to obtain any residual stress results distribution as shown in Figure 5.12 and 5.13. In Figure 5.13 results did not obtain any residual stress. Therefore, module B was used to get residual stress distribution. The residual stress results distribution is shown in MPa terms of Von Mises, loaded and unloaded results are shown in Figure 5.14, 5.15 respectively.

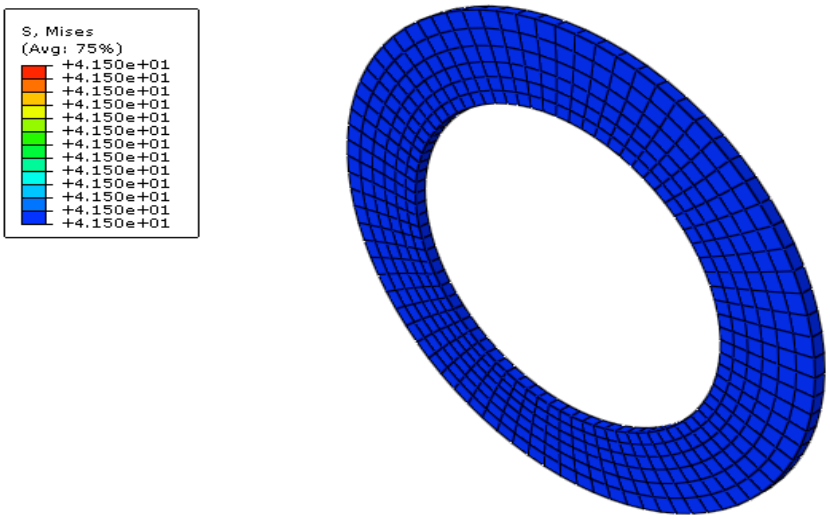

Figure 5:12: Module A, loading Von Mises result.

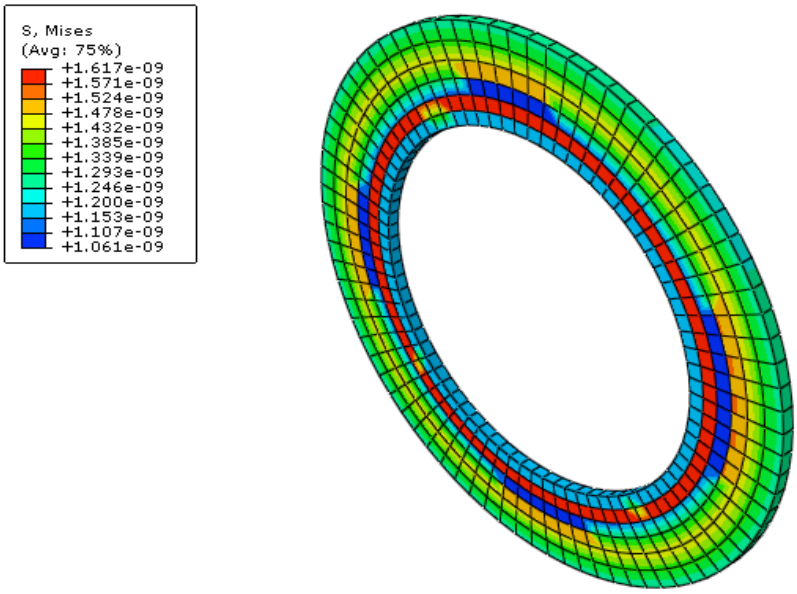

Figure 5:13: Module A , unloading Von Mises result.

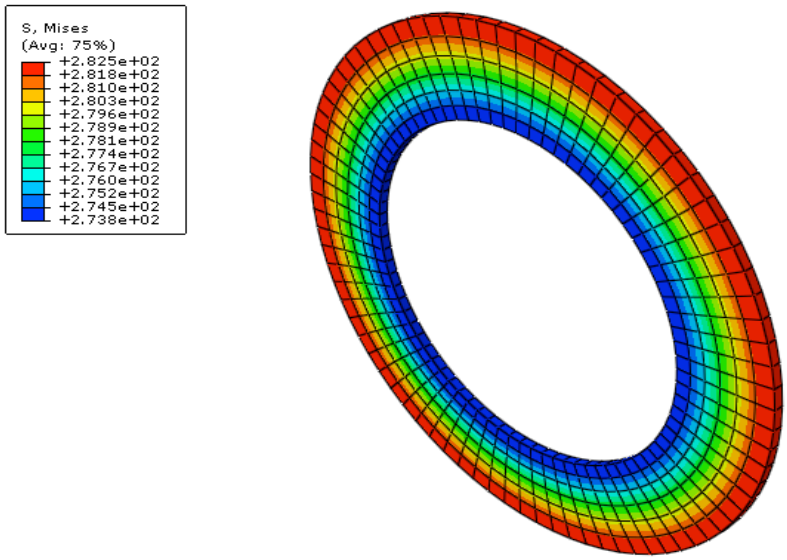

Figure 5:14: Module B, loading Von Mises result.

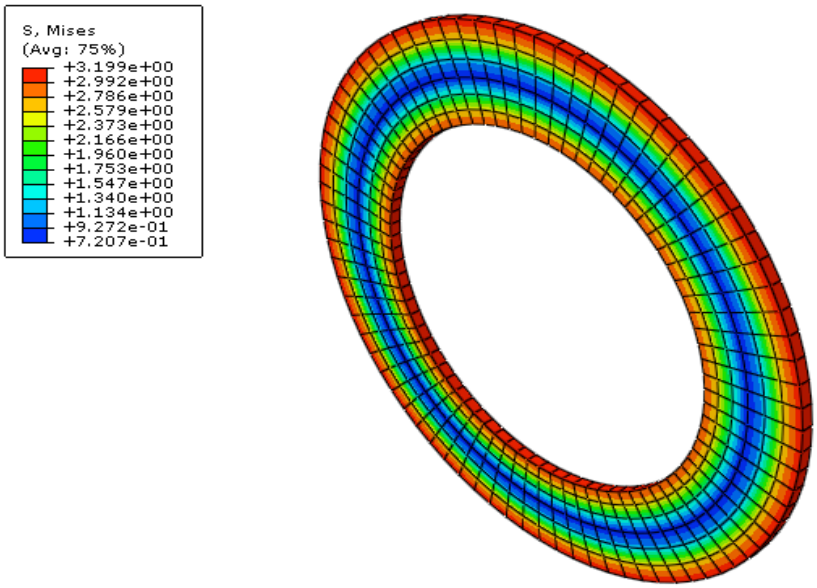

Figure 5:15: Module B, unloading Von Mises result (residual stress).

5.7 Discussions and Conclusion

In this study the effect of residual stress distribution on a thin, circular plate was investigated. The main objective of this study was to compare residual macro stresses on two steel cold-rolled alloys of AISI 1020 specimens, which were loaded and unloaded using two-dimensional X-ray diffraction. For specimen unloading 1, the residual stresses using two-dimensional X-ray diffraction were σ_{11} = 240 ± 24 MPa and σ_{22} = 252.5±21.224 MPa. In addition, for specimen 2 which was loaded by uniform compressive pressure of 41.5 MPa, the residual stresses were σ_{11}= 285 ± 20 MPa and σ_{22} = 219.3±20.424 MPa. As a result, the differences in residual stresses in the thin, circular plates between specimens 1 and 2 could have occurred because of the external load of 41.5MPa, which added to σ_{11} specimens 2. However, specimens 1 and 2 had high residual stress distribution due to cold rolled manufacturing processing. Specimen 2 could differ from specimen 1 due to external load; however, the external load of 41.5 MPa was not enough itself to reach the plastic region.

Therefore, comparing modules A and B proved finite element analysis. In module A, compressive pressure of 41.5 MPa was applied in specimen 2, which was not enough to deform and reach the plastic region; therefore, no residual stress was found. Consequently, the amount of pressure was increased for module B to 300 MPa to reach plastic region and to obtain residual stress distribution.

In short, applying compressive pressure of 41.5 MPa was not enough in itself to obtain residual stress; therefore, the residual stress in the experiment was due to cold rolled manufacturing processing and not because of external load. In order to obtain residual stresses due to external

load rather than manufacturing processing, the researcher must increase the amount of pressure at least to 300 MPa for specimen 2.

Notably, a three-dimensional finite element model was used rather than a two-dimensional model because it covered all geometrical effects. Also, the three-dimensional finite element model had the ability to predict the pressure on the top surfaces of the specimens rather than on their edges.

This work conducted an analysis of the residual stress effect on a material, and the effect of an external loading on a material was shown. There are two identical thin circular plates in this research, which analyzed the effect of residual stress.

5.8 Future work

In addition to this work the fatigue test may be used to estimate the fatigue life of the material. Also, instead of using a statics load to the specimen, another external effect can be applied such as a heat treatment, welding effect, dynamic loaded and other can investigate. In addition, two-dimensional X-ray diffraction was used to analyze residual stress a the macro level, by which a synchrotron source can provide more accurate information about residual stress [1]. In addition, instead of solid plate used in experiment, a thin film can be investigated or other type of specimens.

Appendix A

Residual stresses specimen 1

09/10/2012 10:56:56 AM
Project: Stress_2D
Operator:
Sample:
Site:

Sample

Material	H K L	Wavelength	2Theta	Poisson	Young	S1	1/2 S2	Arx
Fe	2 1 1	Co-Ka1	99.699	0.280	220264	-1.271E-6	5.811E-6	1.000

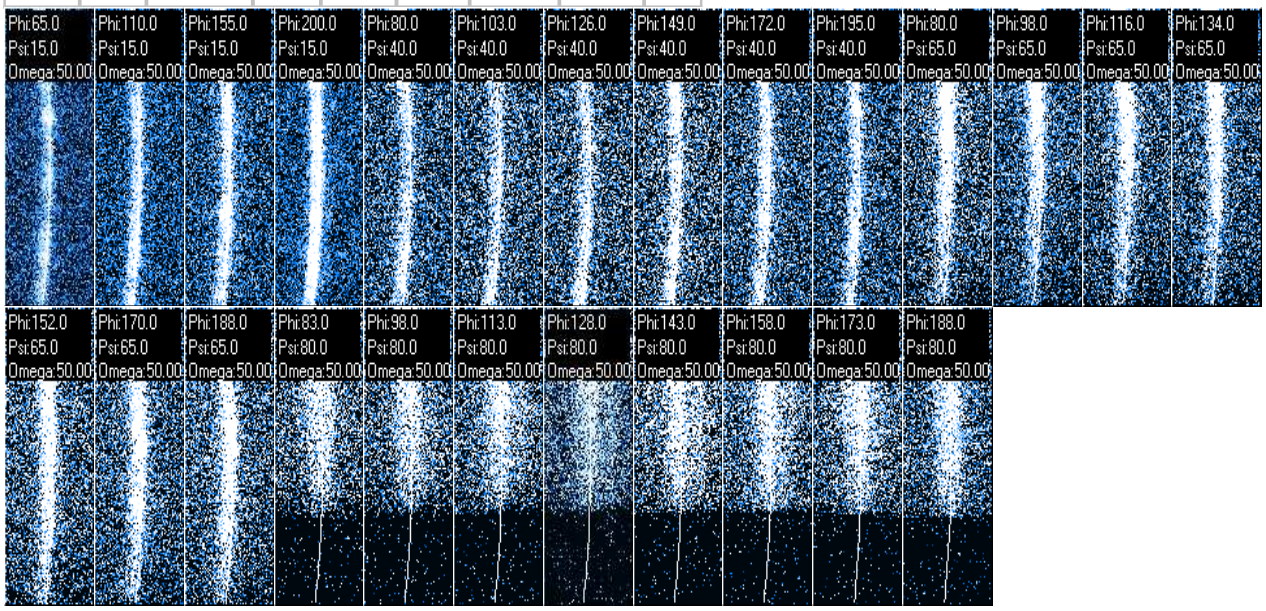

Integration:

2 Thetha start: 101.5
Gamma start: -73.9
Subregions: 10
Peak 20

2 Thetha stop: 97.5
Gamma stop: -106.2
Step: 0.1

1

Measured:	Peak Evaluation Method:	Stress Model:	Pseudo-Hydro:
01-Jul-2012	Pearson VII	Biaxial	0.0 ± 18.8

Normal: 252.5 ± 21.2

Shear: -/- ± -/-

Corrections: Absorption , Background (5) , Polarisation , Smooth , K alpha 2 (0.50)

Stress Tensor:

240.0 ± 24.0	-15.8 ± 19.0	-/- ± -/-
-15.8 ± 19.0	252.5 ± 21.2	-/- ± -/-
-/- ± -/-	-/- ± -/-	-/- ± -/-

Principal Stress Tensor: Sigma I : 263.2 Sigma II : 229.3 Sigma III : -/-

Stress Orientation:

124.2	34.2	-/-
34.2	55.8	-/-
90.0	90.0	-/-

d 0: 0.1171 nm **2 thetha 0:** 99.6410

Data:	Segments:	Omega:	Phi:	Psi:	Gamma:	2Thetha:	Rejection:
	Acusail2f_292-000-0000	50.0	65.0	15.0	-75.505	99.699	
					-78.739	99.701	
					-81.973	99.712	
					-85.207	99.692	
					-88.441	99.704	
					-91.674	99.712	
					-94.908	99.663	
					-98.142	99.692	
					-101.376	99.686	
					-104.610	99.682	

2

Acusail2f_292-000-0001	50.0	110.0	15.0	-75.505	99.699
				-78.739	99.701
				-81.973	99.712
				-85.207	99.692
				-88.441	99.704
				-91.674	99.712
				-94.908	99.663
				-98.142	99.692
				-101.376	99.686
				-104.610	99.682
Acusail2f_292-000-0002	50.0	155.0	15.0	-75.505	99.699
				-78.739	99.701
				-81.973	99.712
				-85.207	99.692
				-88.441	99.704
				-91.674	99.712
				-94.908	99.663
				-98.142	99.692
				-101.376	99.686
				-104.610	99.682
Acusail2f_292-000-0003	50.0	200.0	15.0	-75.505	99.699
				-78.739	99.701
				-81.973	99.712
				-85.207	99.692
				-88.441	99.704
				-91.674	99.712
				-94.908	99.663
				-98.142	99.692
				-101.376	99.686
				-104.610	99.682

Acusail2f_293-000-0000	50.0	80.0	40.0	-75.505	99.699
				-78.739	99.701
				-81.973	99.712
				-85.207	99.692
				-88.441	99.704
				-91.674	99.712
				-94.908	99.663
				-98.142	99.692
				-101.376	99.686
				-104.610	99.682
Acusail2f_293-000-0001	50.0	103.0	40.0	-75.505	99.699
				-78.739	99.701
				-81.973	99.712
				-85.207	99.692
				-88.441	99.704
				-91.674	99.712
				-94.908	99.663
				-98.142	99.692
				-101.376	99.686
				-104.610	99.682
Acusail2f_293-000-0002	50.0	126.0	40.0	-75.505	99.699
				-78.739	99.701
				-81.973	99.712
				-85.207	99.692
				-88.441	99.704
				-91.674	99.712
				-94.908	99.663
				-98.142	99.692
				-101.376	99.686
				-104.610	99.682

4

Acusail2f_293-000-0003	50.0	149.0	40.0	-75.505	99.699
				-78.739	99.701
				-81.973	99.712
				-85.207	99.692
				-88.441	99.704
				-91.674	99.712
				-94.908	99.663
				-98.142	99.692
				-101.376	99.686
				-104.610	99.682
Acusail2f_293-000-0004	50.0	172.0	40.0	-75.505	99.699
				-78.739	99.701
				-81.973	99.712
				-85.207	99.692
				-88.441	99.704
				-91.674	99.712
				-94.908	99.663
				-98.142	99.692
				-101.376	99.686
				-104.610	99.682
Acusail2f_293-000-0005	50.0	195.0	40.0	-75.505	99.699
				-78.739	99.701
				-81.973	99.712
				-85.207	99.692
				-88.441	99.704
				-91.674	99.712
				-94.908	99.663
				-98.142	99.692
				-101.376	99.686
				-104.610	99.682

5

Acusail2f_294-000-0000	50.0	80.0	65.0	-75.505	99.699
				-78.739	99.701
				-81.973	99.712
				-85.207	99.692
				-88.441	99.704
				-91.674	99.712
				-94.908	99.663
				-98.142	99.692
				-101.376	99.686
				-104.610	99.682
Acusail2f_294-000-0001	50.0	98.0	65.0	-75.505	99.699
				-78.739	99.701
				-81.973	99.712
				-85.207	99.692
				-88.441	99.704
				-91.674	99.712
				-94.908	99.663
				-98.142	99.692
				-101.376	99.686
				-104.610	99.682
Acusail2f_294-000-0002	50.0	116.0	65.0	-75.505	99.699
				-78.739	99.701
				-81.973	99.712
				-85.207	99.692
				-88.441	99.704
				-91.674	99.712
				-94.908	99.663
				-98.142	99.692
				-101.376	99.686
				-104.610	99.682

6

Acusail2f_294-000-0003	50.0	134.0	65.0	-75.505	99.699
				-78.739	99.701
				-81.973	99.712
				-85.207	99.692
				-88.441	99.704
				-91.674	99.712
				-94.908	99.663
				-98.142	99.692
				-101.376	99.686
				-104.610	99.682
Acusail2f_294-000-0004	50.0	152.0	65.0	-75.505	99.699
				-78.739	99.701
				-81.973	99.712
				-85.207	99.692
				-88.441	99.704
				-91.674	99.712
				-94.908	99.663
				-98.142	99.692
				-101.376	99.686
				-104.610	99.682
Acusail2f_294-000-0005	50.0	170.0	65.0	-75.505	99.699
				-78.739	99.701
				-81.973	99.712
				-85.207	99.692
				-88.441	99.704
				-91.674	99.712
				-94.908	99.663
				-98.142	99.692
				-101.376	99.686
				-104.610	99.682

7

Acusail2f_294-000-0006	50.0	188.0	65.0	-75.505	99.699
				-78.739	99.701
				-81.973	99.712
				-85.207	99.692
				-88.441	99.704
				-91.674	99.712
				-94.908	99.663
				-98.142	99.692
				-101.376	99.686
				-104.610	99.682
Acusail2f_295-000-0000	50.0	83.0	80.0	-75.505	99.699
				-78.739	99.701
				-81.973	99.712
				-85.207	99.692
				-88.441	99.704
				-91.674	99.712
				-94.908	99.663
				-98.142	99.692
				-101.376	99.686
				-104.610	99.682
Acusail2f_295-000-0001	50.0	98.0	80.0	-75.505	99.699
				-78.739	99.701
				-81.973	99.712
				-85.207	99.692
				-88.441	99.704
				-91.674	99.712
				-94.908	99.663
				-98.142	99.692
				-101.376	99.686
				-104.610	99.682

8

Acusail2f_295-000-0002	50.0	113.0	80.0	-75.505	99.699
				-78.739	99.701
				-81.973	99.712
				-85.207	99.692
				-88.441	99.704
				-91.674	99.712
				-94.908	99.663
				-98.142	99.692
				-101.376	99.686
				-104.610	99.682
Acusail2f_295-000-0003	50.0	128.0	80.0	-75.505	99.699
				-78.739	99.701
				-81.973	99.712
				-85.207	99.692
				-88.441	99.704
				-91.674	99.712
				-94.908	99.663
				-98.142	99.692
				-101.376	99.686
				-104.610	99.682
Acusail2f_295-000-0004	50.0	143.0	80.0	-75.505	99.699
				-78.739	99.701
				-81.973	99.712
				-85.207	99.692
				-88.441	99.704
				-91.674	99.712
				-94.908	99.663
				-98.142	99.692
				-101.376	99.686
				-104.610	99.682

Acusail2f_295-000-0005	50.0	158.0	80.0	-75.505	99.699
				-78.739	99.701
				-81.973	99.712
				-85.207	99.692
				-88.441	99.704
				-91.674	99.712
				-94.908	99.663
				-98.142	99.692
				-101.376	99.686
				-104.610	99.682
Acusail2f_295-000-0006	50.0	173.0	80.0	-75.505	99.699
				-78.739	99.701
				-81.973	99.712
				-85.207	99.692
				-88.441	99.704
				-91.674	99.712
				-94.908	99.663
				-98.142	99.692
				-101.376	99.686
				-104.610	99.682
Acusail2f_295-000-0007	50.0	188.0	80.0	-75.505	99.699
				-78.739	99.701
				-81.973	99.712
				-85.207	99.692
				-88.441	99.704
				-91.674	99.712
				-94.908	99.663
				-98.142	99.692
				-101.376	99.686
				-104.610	99.682

10

Appendix B

Residual stresses specimen 2

09/10/2012 10:49:58 AM
Project: Stress_2D
Operator:
Sample:
Site:

Sample

Material	H K L	Wavelength	2Theta	Poisson	Young	S1	1/2 S2	Arx
Fe	2 1 1	Co-Ka1	99.699	0.280	220264	-1.271E-6	5.811E-6	1.000

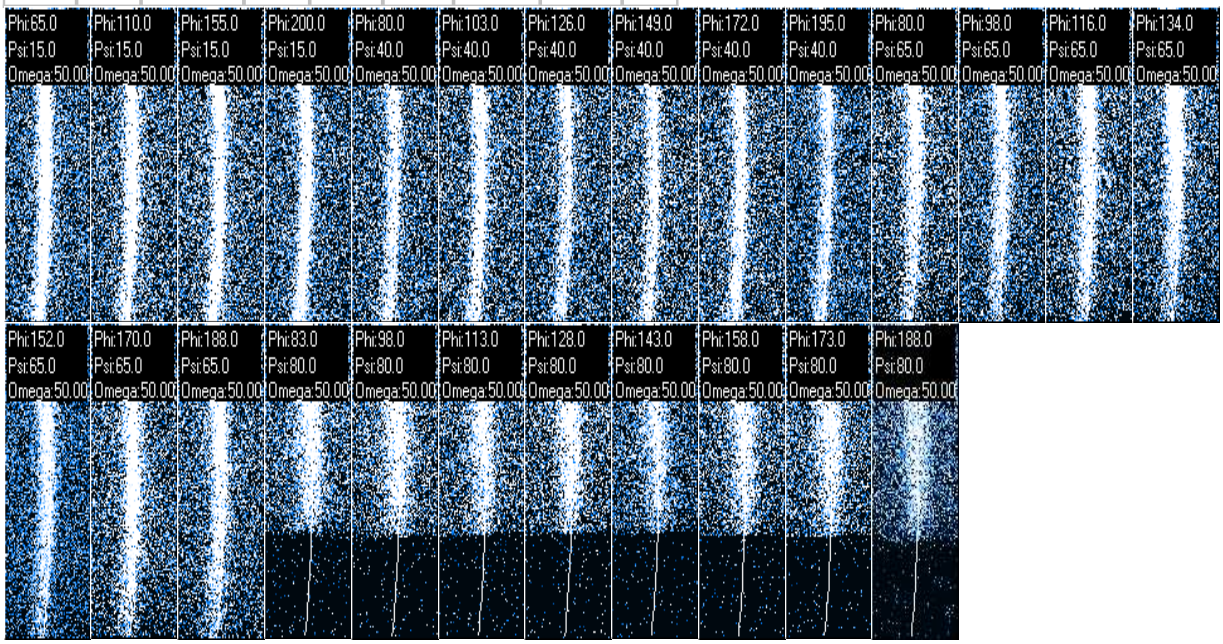

Integration:
2 Thetha start: 101.5
Gamma start: -73.9
Subregions: 10
Peak 20
2 Thetha stop: 97.5
Gamma stop: -106.2
Step: 0.1

1

Measured:	Peak Evaluation Method:	Stress Model:	Pseudo-Hydro:
01-Jul-2012	Pearson VII	Biaxial	0.0 ± 18.1
		Normal:	
		285.1 ± 20.0	
		Shear:	
		-/- ± -/-	

Corrections: Absorption , Background (5) , Polarisation , Smooth , K alpha 2 (0.50)

Stress Tensor:

285.1 ± 20.0	-4.8 ± 15.8	-/- ± -/-
-4.8 ± 15.8	219.3 ± 20.4	-/- ± -/-
-/- ± -/-	-/- ± -/-	-/- ± -/-

Principal Stress Tensor: Sigma I : 285.4 Sigma II : 218.9 Sigma III : -/-

Stress Orientation:

4.1	85.9	-/-
94.1	4.1	-/-
90.0	90.0	-/-

d 0: 0.1171 nm **2 thetha 0:** 99.6375

Data:	Segments:	Omega:	Phi:	Psi:	Gamma:	2Thetha:	Rejection:
	Acusail1f_296-000-0000	50.0	65.0	15.0	-75.505	99.721	
					-78.739	99.691	
					-81.973	99.701	
					-85.207	99.693	
					-88.441	99.694	
					-91.674	99.693	
					-94.908	99.683	
					-98.142	99.683	
					-101.376	99.680	
					-104.610	99.674	

2

Acusail1f_296-000-0001	50.0	110.0	15.0	-75.505	99.721
				-78.739	99.691
				-81.973	99.701
				-85.207	99.693
				-88.441	99.694
				-91.674	99.693
				-94.908	99.683
				-98.142	99.683
				-101.376	99.680
				-104.610	99.674
Acusail1f_296-000-0002	50.0	155.0	15.0	-75.505	99.721
				-78.739	99.691
				-81.973	99.701
				-85.207	99.693
				-88.441	99.694
				-91.674	99.693
				-94.908	99.683
				-98.142	99.683
				-101.376	99.680
				-104.610	99.674
Acusail1f_296-000-0003	50.0	200.0	15.0	-75.505	99.721
				-78.739	99.691
				-81.973	99.701
				-85.207	99.693
				-88.441	99.694
				-91.674	99.693
				-94.908	99.683
				-98.142	99.683
				-101.376	99.680
				-104.610	99.674

3

Acusail1f_297-000-0000	50.0	80.0	40.0	-75.505	99.721
				-78.739	99.691
				-81.973	99.701
				-85.207	99.693
				-88.441	99.694
				-91.674	99.693
				-94.908	99.683
				-98.142	99.683
				-101.376	99.680
				-104.610	99.674
Acusail1f_297-000-0001	50.0	103.0	40.0	-75.505	99.721
				-78.739	99.691
				-81.973	99.701
				-85.207	99.693
				-88.441	99.694
				-91.674	99.693
				-94.908	99.683
				-98.142	99.683
				-101.376	99.680
				-104.610	99.674
Acusail1f_297-000-0002	50.0	126.0	40.0	-75.505	99.721
				-78.739	99.691
				-81.973	99.701
				-85.207	99.693
				-88.441	99.694
				-91.674	99.693
				-94.908	99.683
				-98.142	99.683
				-101.376	99.680
				-104.610	99.674

Acusail1f_297-000-0003	50.0	149.0	40.0	-75.505	99.721
				-78.739	99.691
				-81.973	99.701
				-85.207	99.693
				-88.441	99.694
				-91.674	99.693
				-94.908	99.683
				-98.142	99.683
				-101.376	99.680
				-104.610	99.674
Acusail1f_297-000-0004	50.0	172.0	40.0	-75.505	99.721
				-78.739	99.691
				-81.973	99.701
				-85.207	99.693
				-88.441	99.694
				-91.674	99.693
				-94.908	99.683
				-98.142	99.683
				-101.376	99.680
				-104.610	99.674
Acusail1f_297-000-0005	50.0	195.0	40.0	-75.505	99.721
				-78.739	99.691
				-81.973	99.701
				-85.207	99.693
				-88.441	99.694
				-91.674	99.693
				-94.908	99.683
				-98.142	99.683
				-101.376	99.680
				-104.610	99.674

5

Acusail1f_298-000-0000	50.0	80.0	65.0	-75.505	99.721
				-78.739	99.691
				-81.973	99.701
				-85.207	99.693
				-88.441	99.694
				-91.674	99.693
				-94.908	99.683
				-98.142	99.683
				-101.376	99.680
				-104.610	99.674
Acusail1f_298-000-0001	50.0	98.0	65.0	-75.505	99.721
				-78.739	99.691
				-81.973	99.701
				-85.207	99.693
				-88.441	99.694
				-91.674	99.693
				-94.908	99.683
				-98.142	99.683
				-101.376	99.680
				-104.610	99.674
Acusail1f_298-000-0002	50.0	116.0	65.0	-75.505	99.721
				-78.739	99.691
				-81.973	99.701
				-85.207	99.693
				-88.441	99.694
				-91.674	99.693
				-94.908	99.683
				-98.142	99.683
				-101.376	99.680
				-104.610	99.674

6

Acusail1f_298-000-0006	50.0	188.0	65.0	-75.505	99.721
				-78.739	99.691
				-81.973	99.701
				-85.207	99.693
				-88.441	99.694
				-91.674	99.693
				-94.908	99.683
				-98.142	99.683
				-101.376	99.680
				-104.610	99.674
Acusail1f_299-000-0000	50.0	83.0	80.0	-75.505	99.721
				-78.739	99.691
				-81.973	99.701
				-85.207	99.693
				-88.441	99.694
				-91.674	99.693
				-94.908	99.683
				-98.142	99.683
				-101.376	99.680
				-104.610	99.674
Acusail1f_299-000-0001	50.0	98.0	80.0	-75.505	99.721
				-78.739	99.691
				-81.973	99.701
				-85.207	99.693
				-88.441	99.694
				-91.674	99.693
				-94.908	99.683
				-98.142	99.683
				-101.376	99.680
				-104.610	99.674

8

Acusail1f_298-000-0003	50.0	134.0	65.0	-75.505	99.721
				-78.739	99.691
				-81.973	99.701
				-85.207	99.693
				-88.441	99.694
				-91.674	99.693
				-94.908	99.683
				-98.142	99.683
				-101.376	99.680
				-104.610	99.674
Acusail1f_298-000-0004	50.0	152.0	65.0	-75.505	99.721
				-78.739	99.691
				-81.973	99.701
				-85.207	99.693
				-88.441	99.694
				-91.674	99.693
				-94.908	99.683
				-98.142	99.683
				-101.376	99.680
				-104.610	99.674
Acusail1f_298-000-0005	50.0	170.0	65.0	-75.505	99.721
				-78.739	99.691
				-81.973	99.701
				-85.207	99.693
				-88.441	99.694
				-91.674	99.693
				-94.908	99.683
				-98.142	99.683
				-101.376	99.680
				-104.610	99.674

7

Acusail1f_299-000-0002	50.0	113.0	80.0	-75.505	99.721
				-78.739	99.691
				-81.973	99.701
				-85.207	99.693
				-88.441	99.694
				-91.674	99.693
				-94.908	99.683
				-98.142	99.683
				-101.376	99.680
				-104.610	99.674
Acusail1f_299-000-0003	50.0	128.0	80.0	-75.505	99.721
				-78.739	99.691
				-81.973	99.701
				-85.207	99.693
				-88.441	99.694
				-91.674	99.693
				-94.908	99.683
				-98.142	99.683
				-101.376	99.680
				-104.610	99.674
Acusail1f_299-000-0004	50.0	143.0	80.0	-75.505	99.721
				-78.739	99.691
				-81.973	99.701
				-85.207	99.693
				-88.441	99.694
				-91.674	99.693
				-94.908	99.683
				-98.142	99.683
				-101.376	99.680
				-104.610	99.674

9

Acusail1f_299-000-0005	50.0	158.0	80.0	-75.505	99.721
				-78.739	99.691
				-81.973	99.701
				-85.207	99.693
				-88.441	99.694
				-91.674	99.693
				-94.908	99.683
				-98.142	99.683
				-101.376	99.680
				-104.610	99.674
Acusail1f_299-000-0006	50.0	173.0	80.0	-75.505	99.721
				-78.739	99.691
				-81.973	99.701
				-85.207	99.693
				-88.441	99.694
				-91.674	99.693
				-94.908	99.683
				-98.142	99.683
				-101.376	99.680
				-104.610	99.674
Acusail1f_299-000-0007	50.0	188.0	80.0	-75.505	99.721
				-78.739	99.691
				-81.973	99.701
				-85.207	99.693
				-88.441	99.694
				-91.674	99.693
				-94.908	99.683
				-98.142	99.683
				-101.376	99.680
				-104.610	99.674

10

Bibliography

1. Rossini, N.S., et al., *Methods of measuring residual stresses in components.* Materials & Design, 2012. **35**(0): p. 572-588.

2. He1, B.B., et al., *Two-dimensional X-ray Diffraction for Structure and Stress Analysis.* Materials Science Forum Vols, 2005.

3. Baoping Bob He, U. Preckwinkel, and K.L. Smith, *FUNDAMENTALS OF TWO-DIMENSIONAL X-RAY DIFFRACTION (XRD2).* International Centre for Diffraction, 2000. **Advances in X-ray Analysis,Vol.43**.

4. Cullity, B.D. and S.R. Stock, *Elements of x-ray diffraction*. 2001: Prentice Hall.

5. Kakani, S.L., *Material Science*. 2006: New Age International.

6. He, B.B., *Introduction to two-dimensional X-ray diffraction.* Powder Diffraction, 2003. **18**(02): p. 71-85.

7. Noyan, I.C. and J.B. Cohen, *Residual stress: measurement by diffraction and interpretation*. 1987: Springer.

8. Bruker AXS., *LEPTO DIFFRAC plus LEPTOS Use Manual* 2009, .

9. Lu, J. and S.f.E. Mechanics, *Handbook of measurement of residual stresses*. 1996: Fairmont Press.

10. 1Bob He. and B.A. In, *XRD2 Stress, Analysis Using the VÅNTEC-500.* A. 2012, .

11. Quek, S.S. and G.R. Liu, *Finite Element Method: A Practical Course: A Practical Course*. 2003: Elsevier Science.

12. Hibbitt., Karlsson., and and Sorensen Inc, *ABAQUS user's manual*. A. 2012.

13. Systèmes, D., *Getting Started with Abaqus, Keywords Edition* 2010.

14. J.D. Almer, J.B. Cohen1, and B. Moran, *The effects of residual macrostresses and microstresses on fatigue crack initiation.* Materials Science and Engineering, 2000.

15. Martins, J.A., L.P. Cardoso, and J.A. Fraymann, *Analyses of residual stresses on stamped valves by X-ray diffraction and finite elements method.* Journal of Materials Processing Technology, 2006.

16. Robinson, J.S., et al., *Measurement and Prediction of Machining Induced Redistribution of Residual Stress in the Aluminium Alloy 7449.* Experimental Mechanics, 2011.

17. Anderoglu, O., *Residual stress measurement using X-ray diffraction,* in *Mechanical Engineering* 2004, Texas A&M University,.

18. Yuting, junyi, X., *Abaqus simulations of residual stress induced by waterjet peening,* in *Mechanical Engineering* 2012, Blekinge Institute of Technology, Karlskrona Sweden,.

19. http://www.matweb.com/search/datasheetText.aspx?bassnum=M1020A

20. Pertence a, P.R., et al., *Analysis of a new model material for the physical simulation of*
- *metal forming*. Journal of Materials Processing Technology, 1997.